Spin Dependent Nucleon Structure at Intermediate Q^2

by

Peter Unrau

Submitted to the Department of Physics
in partial fulfillment of the requirements for the degree of

Doctor of Philosophy in Physics

at the

MASSACHUSETTS INSTITUTE OF TECHNOLOGY

June 1996

Author ....
Department of Physics
May 17, 1996

Certified by. ....
Xiangdong Ji
Professor
Thesis Supervisor

Accepted by ....
George F. Koster
Chairman, Departmental Committee on Graduate Students

Spin Dependent Nucleon Structure at Intermediate Q^2

by

Peter Unrau

Submitted to the Department of Physics
on May 17, 1996, in partial fulfillment of the
requirements for the degree of
Doctor of Philosophy in Physics

Abstract

This thesis focuses on hadronic spin structure at low and intermediate energies, $0 < Q^2 < 3$ GeV^2. The thesis is divided into two main sections. Each section addresses a different aspect of spin dependent hadronic physics which has not been studied previously in detail.

The first section studies hydrogen hyperfine splitting. A polarizability term depending on the proton's G_1 and G_2 spin dependent structure functions is extracted with a theoretical precision of 0.1 ppm. A detailed reanalysis of the elastic form factor contributions is performed. Important radiative recoil corrections are calculated for the first time. Weak interaction effects are examined and are found to contribute only marginally at the current level of precision. A pion electroproduction parameterization of the existing low energy data data is constructed. The analysis yields a polarizability correction consistent with the value extracted from hyperfine splitting, but quantitative comparison of the extracted polarizability will require data from CEBAF.

The second section studies the effect of higher twists or $1/Q^2$ corrections to the lowest moments of the proton's structure functions. The target mass corrections to the moments of the spin dependent scaling functions g_1 and g_2 are derived. The twist-four corrections to the first moment of G_1 are examined and the magnitude of the effect estimated using the MIT bag model. A continuous parameterization of the moment from low to high Q^2 is constructed. The resulting prediction should be compared with experiment. The interplay between resonance structure and twist corrections at low Q^2 is studied using the spin independent structure function F_2. The twist-four corrections along with estimates of the radiative corrections are extracted from existing data. The analogous analysis for the spin dependent structure functions awaits experimental data.

Thesis Supervisor: Xiangdong Ji
Title: Professor

Nature resolves everything into its
component atoms and never reduces
anything to nothing.

-Lucretius, (c.100 - c.55 B.C.)

Acknowledgments

This thesis could not be finished without many people's generous help. Primarily I would like to thank my supervisor Xiangdong Ji. Xiangdong showed incredible patience with me and always had useful suggestions and approaches to problems. I particularly appreciated the public speaking opportunities he created for me. I would also like to thank Csaba Csáki for vigorous twice weekly squash matches. Derek Fong for teaching me that cooking is not all that difficult. Qiang Liu for philosophical conversations about cultural differences. Ken Olum for letting me try change ringing and many helpful discussions about boats. Marcin Sawicki, my long standing friend, for those great hiking and canoeing trips. Prof. F. Low for letting me help proofread his textbook on Classical Field Theory. Prof. Belcher and Prof. Jaffe for serving on my thesis committee. I would also like to acknowledge the support of a Canadian NSERC scholarship which afforded me considerable academic flexibility. Finally, I would like to thank Michelle, my wife. Her constant support, expert proof reading and incredible tolerance have been greatly appreciated.

Contents

Chapter 1

Introduction

Understanding spin has always been an important and difficult hurdle towards formulating a physical theory. Take for example atomic physics. After Bohr's correspondence principle successfully explained the gross features of atomic spectra, discrepancies due to the electron's fine structure motivated the development of QED. The current situation in hadronic spin physics is perhaps analogous to the days just after the invention of the Bohr atom. Lists of resonances are known and have been classified according to their various properties. Models such as the nonrelativistic quark model or the MIT bag model can predict resonance spectra with reasonable accuracy. The magnetic moments of hadrons can also be calculated to within 10% or so. There is however an important technical difficulty: while the underlying theory is believed to be QCD, systematic calculations using QCD cannot be performed at low energy due to confinement.

This thesis is concerned with the spin dependent structure functions G_1 and G_2 of the nucleon at low and intermediate energy. These structure functions characterize the spin dependent inclusive cross section observed when polarized leptons are scattered off a polarized nucleon. Remarkably little is known about these structure functions experimentally. This is due to the technological difficulty of producing strongly polarized targets and high intensity polarized electron beams. The existing data taken at EMC, SMC, E142, and E143 have provoked much controversy owing in large part to the tantalizingly small kinematic range of each experiment. The next few years will see a wealth of spin dependent data coming from machines such as CEBAF which are dedicated to studying low and intermediate energy spin physics.

We approach the intractability of QCD at low to intermediate energies by using two approaches. Each addresses a different aspect of spin dependent hadronic physics in a energy range which has not been explored in detail. Chapters Two and Three concern the extraction of a low energy hadronic observable called the polarizability from the hyperfine splitting of the $1S_{1/2}$ state in hydrogen. Originally it was hoped that hyperfine splitting would provide a method of obtaining a very accurate test of QED as the hyperfine frequency is known to 6 parts in 10^{13}. However it was soon realized that large hadronic corrections make this impossible and theoretical attention shifted to muonium. This large hadronic correction is actually very interesting as it probes the spin structure of the proton for momentum transfer ranging from m_e to m_p. The hadronic correction can be decomposed into rigid contributions arising from the proton's elastic form factors and the polarizability which represents virtual excitations of the proton. We isolate the polarizability by removing the larger elastic form factor dependence from the hadronic correction. The polarizability is related to G_1 and G_2 through a dispersion like relation. The $Q^2 = 0$ end point of which, corresponds to the Drell Hearn Gerasimov (DHG) sum rule which is being actively investigated at CEBAF. Chapter Two starts by reviewing atomic physics experiments which are sensitive to hadronic structure. The $nS_{1/2}$ states of hydrogen are all sensitive to the proton's mean square charge radius, but are not sensitive to spin structure since the hyperfine structure effects are easily removed from the analysis. The nS states do offer a method of independently estimating the proton size which will be important if the precision of these experiments can be improved. Chapter Three contains the detailed analysis of hydrogen hyperfine splitting. The total hadronic effects are isolated from hyperfine splitting with a relative error of 0.3%. The hadronic corrections depending on the elastic form factors are then calculated to a precision of 1.5%. The error being determined by the elastic form factors. After calculating and removing important QED radiative corrections we isolate a term which we attribute to the proton's polarizability. We find $\delta(\text{pol}) = 2.42(58)$ ppm. The relative error on the polarizability being 23%. This error can in principle be reduced to 5% if more accurate knowledge of the elastic form factors becomes available. The polarizability should be viewed as an important consistency check for high energy experiment. It will be interesting to see whether the spin dependent data collected at for CEBAF will support this number.

The second approach examines the problem of spin at intermediate energies from the opposite end of the energy spectrum. This marks a departure from the atomic physics of the previous chapters. Deep inelastic scattering is introduced in Chapter Four. There are two important classes of corrections which need to be studied at low energies. Radiative corrections, which have a logarithmic dependence on the momentum transfer Q^2, and twist corrections which are of the form $1/Q^2$. Both can be understood using the operator product expansion (OPE) to systematically expand the hadronic bilocal current. At high energies only the radiative corrections are important but at intermediate energies twist corrections must be taken into account. Chapter Five calculates twist-four corrections to the lowest moment of the spin dependent structure function G_1. The corrections resulting from this calculation are interesting as a number of recent experiments have performed spin dependent measurements at low Q^2 where their interpretation is affected by twist corrections. The source of concern is that measurements taken by E142 for example do not saturate the Ellis-Jaffe sum rule for the proton, resulting in what has come to be known as the "spin crisis". The final section, Chapter Six, concerns the duality between resonance physics and the partonic picture used at higher energies. There is an interval in Q^2 where the higher twist corrections can be thought of as arising from the onset of coherent behavior, which derive from the excitation of resonance structures. Using previously measured spin independent observables it is possible to integrate out the resonance structure and to continue using the language of deep inelastic scattering into the resonance region. We extract the twist corrections and radiative correction from data on F_2 and study their behavior.

1.1 Publications

The work in the first section concerning hyperfine splitting, will be submitted to Phys. Rev. D. The material concerning higher twists (Chapters Five and Six), has been published and represents work done in collaboration with my supervisor Xiangdong Ji. The references to this material are,

- X. Ji, P. Unrau, Phys. Lett. B, **333**, 228 (1994).
- X. Ji, P. Unrau, Phys. Rev. D, **52**, 72 (1995).

Chapter 2

Hadronic Structure and Atomic Systems

The hydrogen atom has historically served as a test bed for quantum theory. The advent of new experimental techniques has rekindled the study of atomic systems. In particular, a number of exciting Lamb shift experiments have appeared recently in the literature [1], [2], [3] which are sensitive to the hadronic charge radius. This chapter describes the experimental and theoretical status of current work in this area and comments on planned experiments to measure hadronic structure using muonic atoms. Finally I examine the lowest order tree level contributions to hyperfine splitting including the effects of weak interaction contributions before discussing in detail higher order corrections in Chapter Three.

2.1 Lamb Shifts and Charge Radius

The standard Lamb shift measures the 1057 MHz fine structure transition between the $2S_{1/2}$ and the $2P_{1/2}$ states in hydrogen. While Bohr theory would predict degeneracy between the $2S$ and $2P$ states, spin orbit effects actually split the degeneracy on the $2P$ states, resulting in $2P_{1/2}$ and $2P_{3/2}$ levels. Further radiative corrections push down the $2P_{1/2}$ levels relative to the $2S_{1/2}$ resulting in the classical Lamb shift. While of historical interest, the classic Lamb shift is not the best system to study hadronic effects as hadronic contributions are suppressed by a factor of $1/n^3$ for excited states. The magnitude of the hadronic effect is governed by the degree of overlap between the electron and proton wavefunctions. Since the electron wavefunction at the origin is given by,

$$\Psi_{n,l}(0) = \frac{1}{\sqrt{\pi}}\left(\frac{\alpha m_r}{n}\right)^{\frac{3}{2}}\delta_{l0}, \tag{2.1}$$

the ground state has the largest hadronic contribution. Studying the Lamb shift of the ground state however has been problematic. Only the relatively recent invention of tunable dye lasers has made it possible to study optical transitions between the $1S$ and states with large n to high precision. D.J. Berkeland et al. [1] measured $\Delta\mathrm{E}_{1/2,3/2} = H(2S_{1/2} - 4P_{1/2,3/2}) - \frac{1}{4}H(1S_{1/2} - 2S_{1/2})$ to an accuracy of 6 ppm; the highest precision to date for a Lamb shift experiment. The experiment is quite elegant and involves measuring the beat frequency between the $4P \rightarrow 2S$ and $2S \rightarrow 1S$ transitions. Since the quantity ΔE is zero in Bohr theory, one clearly is measuring important perturbative effects.

Fig. 2-1 shows the relevant levels and some fine structure details. Theoretically, the higher energy states are well understood [4] and the only input from hadronic theory is the proton charge radius. The notion of charge radius is largely historical and we shall use it to easily differentiate between particular elastic form factor parameterizations. We shall always refer to the RMS charge radius using the method of Sachs where,

$$\frac{<r^2>}{6} = -\frac{\partial G_E(Q^2)}{\partial Q^2}|_{Q^2=0}. \tag{2.2}$$

The hadronic correction which effects the $1S$ and $2S$ states can easily be calculated naively where one finds,

$$\Delta\mathrm{E}(n,l) = \frac{2}{3n^3}\alpha^4 m_r^3 <r^2>_p \delta_{l0}. \tag{2.3}$$

This formula also holds for the formal analysis of the energy shift where $G_E^2 - 1$ is Taylor expanded about $Q^2 = 0$ GeV^2 (see for example [5]). There exists in the literature two inconsistent measurements of the charge radius of the proton: the

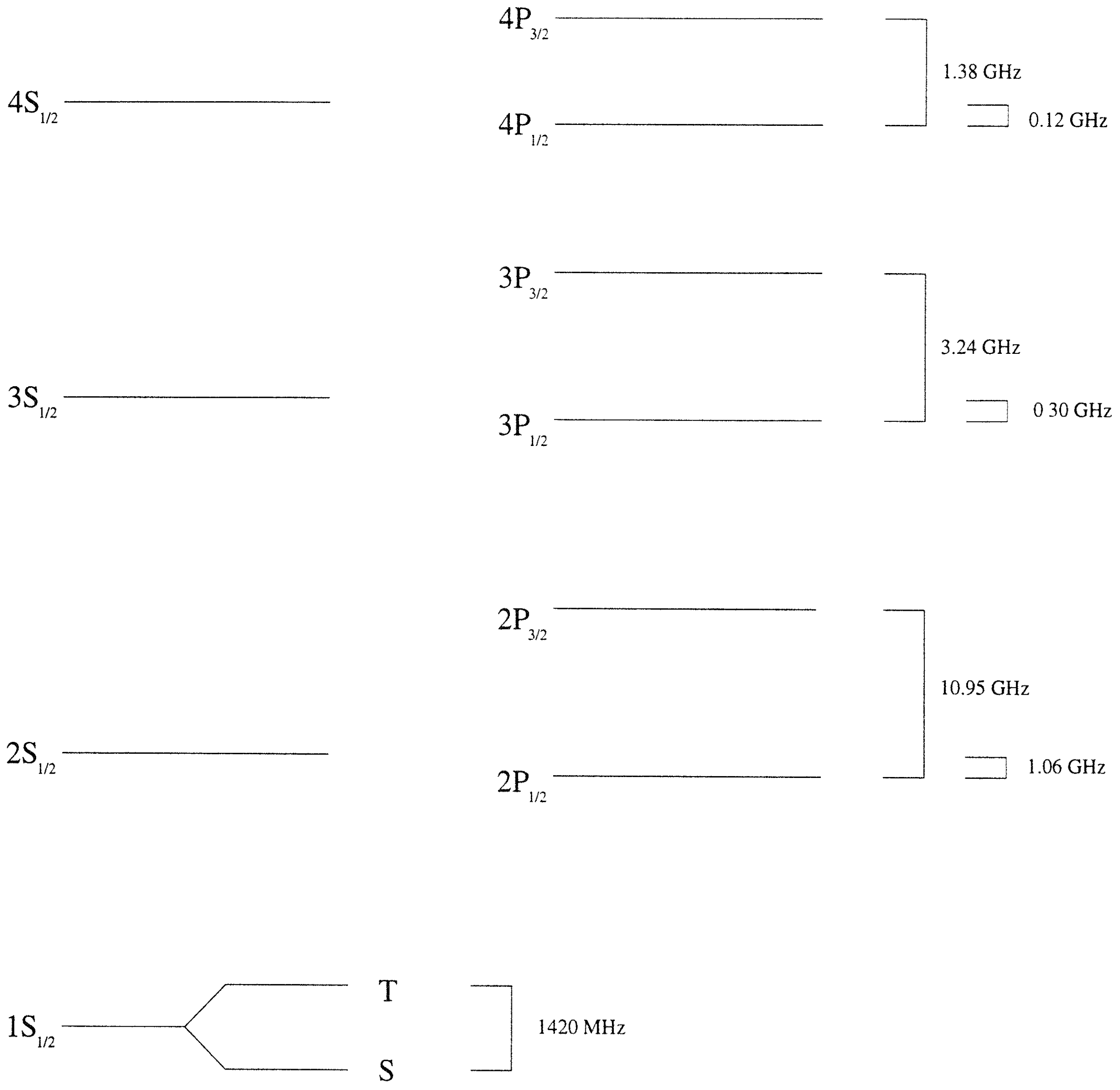

Figure 2-1: The lowest excitations in hydrogen. Orbitals higher than P are not shown. Fine structure is indicated in GHz. The triplet (T) and singlet (S) hyperfine states for the ground state are also shown.

older value of 0.805(11) fm measured by L.N. Hand et al. [6] and a more recent measurement of 0.862(12) fm measured by G.G. Simon et al. [7]. The error from the charge radius contributes about half the total 5 ppm uncertainty in the prediction of the $1S$ energy for each charge radius, the remainder being uncalculated QED effects. The systematic errors between the two form factor parameterizations are sufficiently large that the $1S$ Lamb shift measurement can differentiate between them. The $1S$ Lamb shift measurement is entirely consistent with the larger radius. A more careful analysis of Eq. (2.3) that takes into account the Q^2 dependence of the proton's elastic form factors is missing in the literature. This will become essential when the experimental measurement of the $1S$ Lamb shift improves along with QED theory by a factor of five. When this level of precision is reached, one must also take into account the proton's self energy. The result of an analysis by K. Pachucki [5] shifts the $1S$ level upwards by 0.6 ppm, thus in principle more accurate Lamb shift experiments can tightly constrain the mean square charge radius.

2.2 Hyperfine Splitting

Hyperfine splitting results from the magnetic moment interactions between the proton and electron. The standard derivation of the lowest order Fermi hyperfine splitting given in textbooks is in the coordinate representation (see for example Sakurai [8] or Itzykson and Zuber [9]) so for completeness we give the momentum derivation. This exercise provides insight into how reduced mass effects arise and integrates with the higher order corrections which are also given in the momentum representation. The spin independent wave function in the coordinate representation is given by,

$$\Psi(\vec{r}) = \frac{1}{\sqrt{\pi}}(\gamma)^{\frac{3}{2}} e^{-\gamma r}. \tag{2.4}$$

Where $\gamma = \alpha m_r$, α being the fine structure constant and $m_r = \frac{m_e m_p}{m_e + m_p}$ the reduced mass. Fourier transforming we find,

$$\varphi(p) = -(2\pi)^3 i\delta(p_0) \cdot \frac{8\sqrt{\pi}\ \gamma^{\frac{5}{2}}}{(\vec{p}^2 + \gamma^2)^2}. \tag{2.5}$$

the non relativistic nature of the solution being brought to attention by the delta function in energy. Since the electron in hydrogen is only weakly relativistic ($p \approx \alpha m_e$) this is a good starting wavefunction for bound state perturbation theory. The following spin projection operator for the electron and proton,

$$A(p) = \left(\frac{2m + p_i\gamma^i}{2m}\right)\left(\frac{1+\gamma^0}{2}\right) \tag{2.6}$$

selects the correct non-relativistic spin contribution to hyperfine splitting. The calculation of the lowest order diagram in Fig. 2-2 between particles with no magnetic moment proceeds by evaluating,

$$\mathrm{E_F} = -\int \frac{d^4p}{(2\pi)^4}\frac{d^4p'}{(2\pi)^4}\frac{d^4q}{(2\pi)^4}\ \delta^4(p-p'-q)\ \varphi(p')^\dagger\ \frac{e^2}{q^2+i\epsilon}\ \varphi(p)\cdot S(q, m_e, m_p) \tag{2.7}$$

Where p and p' are the electron momenta and q is the momentum transferred through the photon. P and P' are the proton momenta; the spatial parts being equal and opposite to the electron's. The spin dependent part is given by,

$$S(q, m_e, m_p) = \chi_e^\dagger A^\dagger(p')_e \gamma^0\gamma^\mu A(p)_e \chi_e \otimes \chi_p^\dagger A^\dagger(P')_p \gamma^0\gamma_\mu A(P)_p \chi_p, \tag{2.8}$$

where only the spin-spin interaction need be examined. The important term for the electron resulting from the large component of the four-spinor is,

$$(\sigma \cdot p')\sigma_i + \sigma_i(\sigma \cdot p) \doteq -\, i\epsilon_{ijk} q_j \sigma_k. \tag{2.9}$$

The proton has an analogous term. Averaging over the angular part of $\vec{q}$ we find the hyperfine splitting component is given by $S(q, m_e, m_p) = \frac{8}{3}\frac{\vec{q}^2}{m_e m_p}$. Evaluation of Eq.

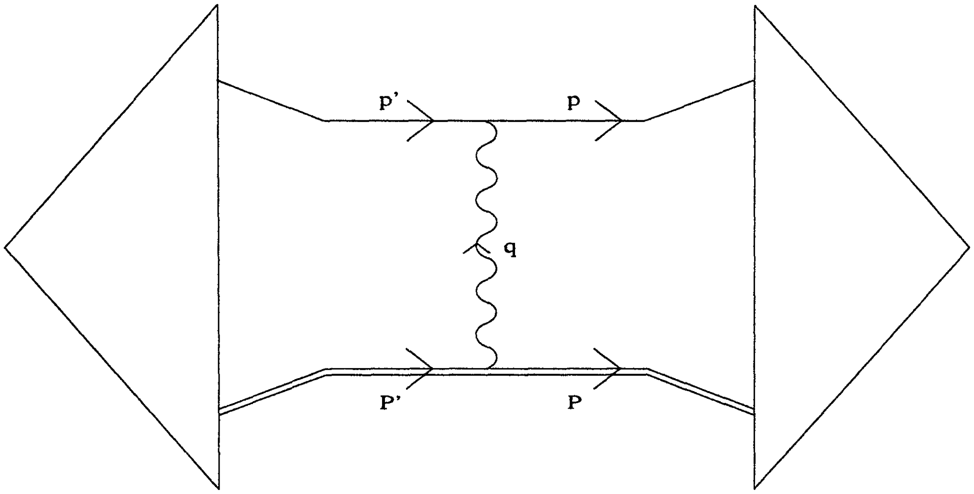

Figure 2-2: The lowest order diagram, where q is the momentum transfer between the proton and electron vertex. The wavefunctions before and after the interaction are represented by the triangles to the left and right.

(2.7) is now straightforward and we find the Fermi result,

$$\mathrm{E_F} = \frac{8}{3}\frac{\alpha^4 m_r^3}{m_e m_p}. \tag{2.10}$$

This result was derived neglecting the magnetic moment at each vertex. The addition of the anomalous moment holds through use of the Gordon identity. The vertex used above; $-ie\gamma^\mu$, must be replaced with

$$\gamma^\mu \to \gamma^\mu + i\kappa\frac{\sigma^{\mu\nu}q_\nu}{2m}, \tag{2.11}$$

where κ is the anomalous magnetic moment of the particle. For the electron this number can be calculated explicitly by studying vertex corrections in QED, while for the proton this number must be taken from experiment. The Gordon identity then yields,

$$\begin{aligned} \gamma^\mu &\to \gamma^\mu(1+\kappa) - \kappa\frac{2p_\mu + q_\mu}{2m} && (2.12) \\ &\doteq \gamma^\mu(1+\kappa). && (2.13) \end{aligned}$$

Where use has been made of the Dirac equation acting on states implied to the left and right of the vertex. The second term in Eq. (2.12) does not contribute to HFS and can be neglected. Thus the full lowest order Fermi calculation for hydrogen is given by,

$$\mathrm{E_F} = \frac{8}{3}\frac{\alpha^4 m_r^3}{m_e m_p}(1+\kappa_p). \tag{2.14}$$

Since the $1+\kappa_e$ term results from QED vertex corrections of the electron line, this correction is traditionally separated from the lowest order Fermi result and grouped with higher order QED corrections.

Higher order corrections to the Fermi result involve hadronic corrections. The most sizable correction in this class involves the proton charge radius, or equivalently, the slope of the proton's magnetic form factor at $Q^2 = 0\ \mathrm{GeV}^2$. The immediate consequence of the new $1S$ Lamb measurement is that it invalidates all previous hyperfine splitting analysis. All previous work has systematically used the smaller charge radius, which, if the Lamb shift result is correct, contain large systematic errors. The smaller radius has been used owing to the early appearance of the standard dipole proton form factors and the relative simplicity of the parameterization. While hyperfine splitting depends only linearly on the charge radius instead of quadratically, the elastic form factors make an important contribution to the hadronic correction which must be understood in order to correctly extract smaller effects such as the polarizability.

Chapter Three treats these corrections in detail. The main point here is that the next set of corrections for the proton are much larger than the nominal $\alpha\beta\ln(1/\beta)$ size which would be predicted for a structureless proton, with $\beta = m_e/m_p$.

2.3 Muonic Systems

The primary reason for studying muonic hydrogen ($\mu^- p$) stems from the $\frac{m_\mu}{m_e}$ enhancement in hadronic signal. The heavier muon has a much smaller Bohr radius and therefore has a much stronger overlap with the proton than the electron system. The life time of the muon however,

$$\tau_\mu = 2.19703(4) \times 10^{-6} \text{ sec} \tag{2.15}$$

makes the actual experiments quite challenging. Not only does one need an accelerator to generate the muon beam, but the muon must also be delivered at thermal energies and in useful quantities before decaying. The muon's short lifetime also means that transitions have a line width of about 145 KHz. The actual transition energies of the muonic system are also awkward to reach using conventional laser technology. Theoretically, electron polarization effects are much stronger than the hydronic case and must be taken into account to higher order.

There are plans to measure the $3D \rightarrow 3P$ transition at PSI (Heidelberg) which will be marginally sensitive to hadronic effects. The dominant corrections being QED vacuum polarization terms as the P and D orbitals do not overlap the proton strongly. Future possibilities include measuring the $2S \rightarrow 2P$ classical Lamb shift analog and the $n = 1$ hyperfine structure, both have large hadronic contributions. The transition frequencies for these experiments are on the order of 40 THz and are apparently barely within reach of current technology.

We close this section by briefly discussing the status of muonium ($\mu^+ e$) hyperfine splitting. Since muonium lacks hadronic structure, QCD contributions are negligible and QED can be used to greater accuracy. The theoretical precision currently is 38 ppb (parts per billion!) the same accuracy as that of the muonic hyperfine measurement itself. Actual comparison between theory and experiment is impossible at this level due to an uncertainty of 300 ppb resulting from the muon mass in the theory input. By comparison, the results of Chapter Three reduce the theoretical uncertainty in hydrogen hyperfine splitting to the 100 ppb level. For additional reviews on muonic systems consult Jungmann, Hughes and Putlitz [10] and for the latest theoretical muonium results see Kinoshita [11].

2.4 Weak Interaction Effects

We estimate the magnitude of weak effects in hydrogen hyperfine splitting. Within the framework of low energy effective theory, the effective Lagrangian for the interaction between electron and proton is given by,

$$
\begin{aligned}
L_{PNC} &= \frac{G_F}{\sqrt{2}} \sum_i \Big(A_i \bar{l} \gamma^\mu \gamma_5 l \cdot \bar{H}_i \gamma_\mu \gamma_5 H_i + B_i \bar{l} \gamma^\mu l \cdot \bar{H}_i \gamma_\mu H_i && (2.16) \\
&+ C_i \bar{l} \gamma^\mu \gamma_5 l \cdot \bar{H}_i \gamma_\mu H_i + D_i \bar{l} \gamma^\mu l \cdot \bar{H}_i \gamma_\mu \gamma_5 H_i \Big). && (2.17)
\end{aligned}
$$

While the V-A (vector-axial) components of this Lagrangian can be measured by parity violating experiments, separating the A-A and V-V from a large QED V-V component can be complicated. Thus the A-A and V-V weak components have not been explicitly measured. If one assumes that the Standard Model gives the axial and vector couplings to the proton, then one can determine the coefficients A_i and B_i.

A computation analogous to the Fermi splitting calculation just previous reveals that only the A-A component of the Fermi interaction contributes to the hyperfine splitting energy.

$$
\begin{aligned}
\delta(\text{Weak}) &= \frac{\mathrm{E}_{\text{Weak}}}{\mathrm{E}_{\mathrm{F}}} = \frac{3}{2} \frac{G_F}{\sqrt{2}} \frac{m_e m_p}{\alpha \pi} \frac{g_A^p}{1+\kappa_p} && (2.18) \\
&\approx 0.117 \text{ ppm}, && (2.19)
\end{aligned}
$$

where $g_A \approx 1.257$ has been used to estimate g_A^p. We will include this estimate when we come to isolate the hadronic terms later next chapter. The weak interaction correction estimated here provides a small correction to the polarizability extracted in Chapter Three.

Chapter 3

Hyperfine Splitting and Hadronic Structure at low Q^2

Hydrogen hyperfine splitting (HFS) contains many layers of physics; on the surface, an atomic physics problem, while underneath a crossroads between QED and the hadronic world of QCD. HFS deals with the coupling between the electron spin and the spin structure of the proton. Unlike muonium, which only has point like spin interactions, the proton's spatial extent and internal spin degrees of freedom must be accounted for. This provides important constraints otherwise only accessible through high energy physics experiments. The goal of this chapter is to understand a subset of these hadronic contributions to better than one part in a million.

The two-photon exchange diagram includes rigid, radiative and polarizability corrections arising from hadron structure effects. The rigid term or coherent recoil requires accurate knowledge of the electric and magnetic form factors obtained from high energy electron beam experiments. This contribution has been extensively reviewed by Bodwin and Yennie [12], who evaluated the recoil corrections using the commonly found dipole parameterization for the form factors. The radiative recoil corrections have not been calculated previously in hydrogen and we find contributions at the level of a part per million. The polarizability effects in the structure calculation result from dispersion integrals over the two spin dependent nucleon structure functions, G_1 and G_2. These structure functions characterize the internal excitations of the proton's spin structure and are measurable in polarized target and beam experiments. Previously the polarizability correction, $\delta(\text{pol})$ was bounded by Gnadig and Kuti who found $|\delta(\text{pol})| < 4$ ppm [13]. This result represents the largest uncertainty in the hadronic theory of HFS. The 4 ppm limit was calculated generously by using the positivity of the total scattering cross section to bound the spin dependent structure functions by the measured spin independent ones.

This chapter provides a fresh outlook on these hadronic corrections to hydrogen hyperfine splitting. We recalculate the rigid contributions using the more sophisticated low energy parameterization of the proton form factors measured by Simon et al. [7]. This serves to eliminate a large systematic error on the order of a few ppm resulting from using the standard dipole form factors. The leading radiative one loop corrections to this result are calculated for the first time. These calculations allow the hadronic polarizability correction to be extracted with a theoretical precision of 0.1 ppm. We find a polarizability contribution of $\delta(pol) = 2.42(56)$ ppm. The dominent source of error results from the error in the elastic form factors. An attempt is made to directly calculate the polarizability correction using currently available spin dependent hadronic data. Pion electroproduction data and recent deep inelastic scattering (DIS) data are used to estimate the size of the polarizability correction. The resulting model is consistent with the bound of Gnadig and Kuti, but the quality of the data is poor and more precise experimental data will be required to make a detailed comparison with our extracted result.

The chapter is divided into five sections. The first section discusses the isolation of the hadronic contribution to the HFS and reviews the known QED contributions in light of recent theoretical advances. The second section outlines how the hadronic structure functions are related to the HFS problem at the one loop level. The third section involves the calculation of the rigid correction, while the fourth and fifth sections deal with the evaluation of the radiative and polarizability corrections respectively.

3.1 The Hadronic Residual

The purpose of this section is to extract as uniquely as possible the hadronic contributions from the measured HFS. By using the existing QED calculation one can extract a hadronic residual which is compared with hadronic calculations. To begin, we define what is meant by a hadronic residual: imagine neglecting all hadronic structure effects except for the mass, charge and magnetic moment. Then in this muonic-like system, one could calculate an expansion in powers of the fine structure constant α and $\beta_p = m_e/m_p$. This expansion would yeild a systematic set of corrections to the lowest order Fermi result. Since this is a bound state problem, logarithms of α and β_p can also appear. Generally two classes of terms will arise: ones which depend only on α, and those which involve both α and β. Within the point-like approximation, the former are called QED corrections and the latter recoil corrections.

The full calculation including all the effects of proton structure will produce a subset of terms which, when the hadronic structure is suppressed, reduce to the recoil terms in the point-like expansion. We group these terms together and call them hadronic corrections. The expansion will still be in powers of β_p but any logarithmic dependence will have shifted to a structure dependent expression. The QED class of corrections to the lowest order term, which depend only on α, remain unchanged and are grouped together as before. Thus the exquisitely measured hyperfine frequency [14] [15], can be decomposed as follows:

$$\begin{aligned} f(\mathrm{HFS})_p &= 1\,420.405\,751\,766\,7(9)\ \mathrm{MHz}[15] \\ &= f_{\mathrm{F}p} + f(\mathrm{QED})_p + f(\mathrm{hadronic})_p, \end{aligned} \tag{3.1}$$

where $f_{\mathrm{F}p}$ is the lowest order Fermi splitting given by,

$$\begin{aligned} f_{\mathrm{F}p} &= \frac{16}{3}\alpha^2 \frac{m_{rp}^3}{m_e^2 m_p} c R_\infty (1+\kappa_p) \\ &= 1\,418.840\,32(13)\ \mathrm{MHz}. \end{aligned} \tag{3.2}$$

Here, m_{rp} is the reduced electron mass in the hydrogen system and κ_p is the anomalous magnetic moment of the proton. This lowest order result sets the maximum numerical accuracy possible from the expansion. In this case, the error is primarily from the value of α. The current precision of 0.1 ppm exceeds the precision possible in current hadronic calculations by about a factor of five, the hadronic error being due primarily to the uncertainty in the charge radius of the proton.

The QED radiative and binding corrections, $f(\mathrm{QED})$, come from the momentum region with $|p_e| < \alpha m_e$. With such low momentum the electron samples only the static dependence of the proton's charge and spin distributions. Since only the corrections which couple the spins of the two particles are of relevance to the HFS problem the result must be proportional to the magnetic moment of the proton and takes the form [12],

$$\begin{aligned} f(\mathrm{QED})_p &= f_{\mathrm{Fp}}\Big[\frac{3}{2}(Z\alpha)^2 + \kappa_e + \alpha(Z\alpha)(\ln 2 - \frac{5}{2}) \\ &- \frac{8\alpha(Z\alpha)^2}{3\pi}\ln(Z\alpha)\Big[\ln(Z\alpha) - 2\ln 2 + \frac{281}{480}\Big] \\ &+ \frac{\alpha(Z\alpha)^2}{\pi}(15.38 \pm 0.29) + \frac{\alpha^2(Z\alpha)}{\pi}D_1\Big]. \end{aligned} \tag{3.3}$$

D_1 represents higher order QED corrections which contribute at the nominal order of 0.124 ppm. Recently T. Kinoshita and M. Nio [11] estimated the D_1 term and found, $D_1 = 0.813 \pm 0.040$.

Subtracting the leading Fermi and QED terms from the experimental splitting isolates the hadronic dependent effects,

$$\frac{f(\mathrm{HFS})_p - f_{\mathrm{F}p} - f(\mathrm{QED})_p}{f_{\mathrm{F}p}} = \delta(\mathrm{hadronic},\mathrm{QED})_p = -32.71\big(10\big)\ \mathrm{ppm}. \tag{3.4}$$

Here we define $\delta(\mathrm{hadronic},\mathrm{QED})_p$ to be the hadronic residual extracted using the α expansion in Eq. (3.3). The next section calculates the dominent hadronic contributions to this residual.

3.2 Structure Function Dependence

The hadronic structure must now be explicitly evaluated and compared to the estimates from the previous section. The term f(hadronic) in Eq. (3.1) contains two-photon exchange diagrams (one loop) with hadronic structure dependence and radiative corrections. Dominant parts of the three-photon exchange diagrams (two loop) have been partially worked out by Bodwin and Yennie [12], which we will also include along with weak interaction contributions. The hadronic term is therefore given by,

$$\delta(\text{hadronic})_p = \delta(\text{one-loop})_p + \delta(\text{one-loop-rad})_p + \delta(\text{two-loop})_p + \delta(\text{weak})_p, \qquad (3.5)$$

where the terms have been placed in decreasing order of importance.

The lowest order correction to the one photon result outlined in Chapter Two is the two-photon exchange or one loop diagram diagram shown in Fig. 3-1. This diagram actually contains within it twice the Fermi splitting. The reason for this over counting stems from the lowest order calculation and resultant choice of kernel. The non-relativistic wavefunction can in principle be obtained by summing to all orders in the ladder approximation purely space-like interactions. If the time-like component is set to zero in either of the photon legs in the one loop diagram, it reduces in this scheme to the one-photon calculation. The one loop diagram therefore contains twice the Fermi splitting (revealed when the time-like component is set to zero in either of the photon legs) which must be subtracted off to give the correct one loop contribution. This diagram is greatly simplified by the following approximation: since the proton's momentum scale is vastly higher than that of the electron's, the two photons must have equal and opposite momentum on the proton's scale. Otherwise the electronic wavefunction would not be able to absorb the resulting momentum transfer. This implies that the spin dependent part of the forward Compton scattering

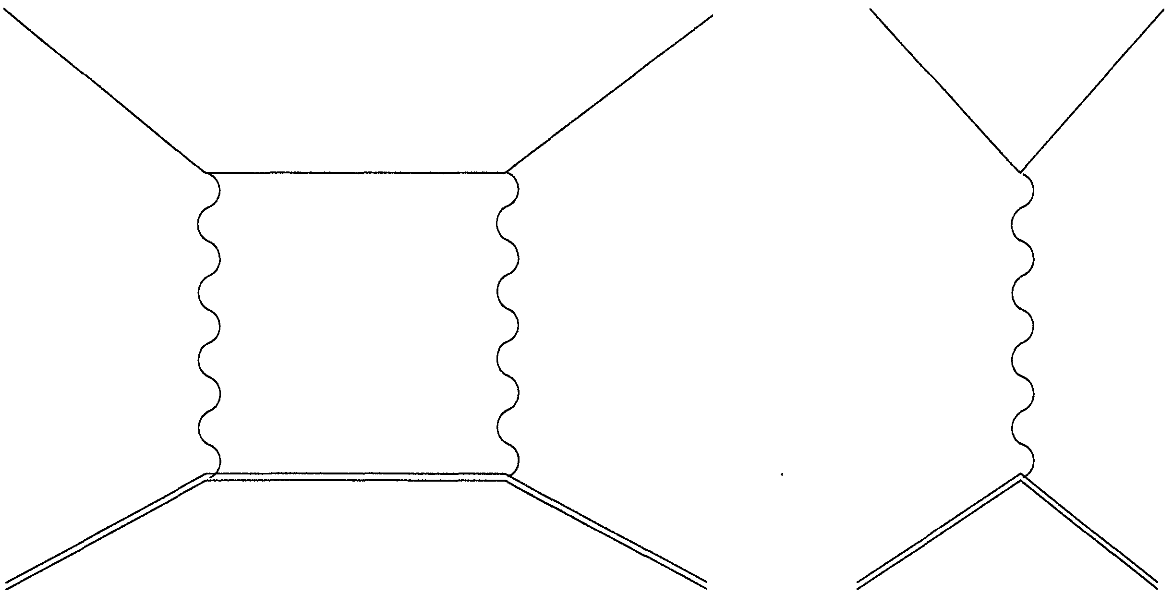

Figure 3-1: The two photon exchange diagram, with crossed diagram suppressed. The single photon diagram must be subtracted to prevent over counting.

amplitude $T_A^{\mu\nu}$ can be used to describe the proton side of the diagram:

$$T_A^{\mu\nu}(\nu, Q^2) = -i\epsilon^{\mu\nu\alpha\beta} q_\alpha \left(s_\beta \frac{S_1(\nu, Q^2)}{m_p^2} + \Big((p\cdot q)s_\beta - (s\cdot q)p_\beta\Big) \frac{S_2(\nu, Q^2)}{m_p^4} \right), \quad (3.6)$$

S_1 and S_2 are the two spin dependent structure functions, q_μ is the momentum of the incident photon and p_μ and s_μ are the proton's incident momentum and spin ($\epsilon^{0123} = 1$). The traditional high energy kinematic variables are given by $\nu = (p\cdot q)/m_p$ and $Q^2 = -q^2$. For an excellent review of the spin dependent structure functions consult Hughes and Kuti [16]. The Compton amplitudes S_i can then be related by a dispersion relation to the absorptive parts G_i,

$$S_1(\nu, Q^2) = -\frac{4F_1\big(F_1 + F_2\big)Q^2}{4(m_p\nu)^2 - Q^4} m_p^2 + 4\int_{\nu_{th}}^{\infty} \frac{\nu' d\nu'}{\nu'^2 - \nu^2} G_1(\nu', Q^2). \quad (3.7)$$

$$S_2(\nu, Q^2) = \frac{4F_2\big(F_1 + F_2\big)(m_p\nu)}{4(m_p\nu)^2 - Q^4} m_p^2 + 4\int_{\nu_{th}}^{\infty} \frac{\nu d\nu'}{\nu'^2 - \nu^2} G_2(\nu', Q^2). \quad (3.8)$$

The G_i are measurable in spin dependent inclusive electroproduction experiments. The terms in front of the integrals take into account elastic scattering; F_1 and F_2 are the Dirac and Pauli form factors. The pion threshold ν_{th} is a function of Q^2. The forward Compton amplitude can also be defined for the electron which to lowest order in QED yields:

$$S_1^e(\nu, Q^2) = \frac{4Q^2}{Q^4 - 4(m_e\nu)^2} m_e^2 \tag{3.9}$$

$$S_2^e(\nu, Q^2) = 0. \tag{3.10}$$

The calculation of corrections to the lowest order Fermi result consists of perturbation theory about the non-relativistic solution. The characteristic momentum scale αm_e of the electron wavefunction seperates from the region of interest, which runs from m_e to m_p, weighting the calculation by the electron density at the origin. By selecting the hyperfine splitting component of the spin-spin interaction the one-loop graphs represent,

$$\delta(\text{one-loop}) = \frac{i\ |\Psi(0)|^2}{2\mathrm{E_F}} \int \frac{d^4q}{(2\pi)^4} \{T_H^{\mu\nu}\ T^e_{\mu\nu}\} \frac{-ie^2}{q^2 + i\epsilon}\, \frac{-ie^2}{q^2 + i\epsilon}, \tag{3.11}$$

the { } mean to extract the HFS component. After extracting the HFS component we find,

$$\delta(\text{one-loop}) = \frac{\Omega}{2\pi^2} \cdot \int \frac{d^4q}{i \cdot q^2(q^4 - 4(m_e\nu)^2)} \left((\nu^2 + 2q^2)S_1 + \frac{3\nu q^2}{m_p} S_2 \right) \tag{3.12}$$

where S_1 and S_2 are the proton structure functions. A rotation to Euclidean space is performed using the transformation: $\nu \longrightarrow iq_4$, $q^2 \longrightarrow Q^2 = \vec{q}^2 + q_4^2$. Subtracting a piece which represents the over counting of the lowest order Fermi result gives the total one loop contribution which is further decomposed into rigid and polarizability corrections:

$$\begin{aligned} \delta(\text{one-rigid})_p \;=\; & \frac{8m_p^2\Omega}{\pi} \int_0^\infty dq_4 d|\vec{q}|\ \vec{q}^2 \cdot \Bigg[\frac{G_M\Big(3q_4^2 G_M + 2\vec{q}^2 F_1\Big)}{\Big(Q^4 + 4m_e^2 q_4^2\Big) \cdot \Big(Q^4 + 4m_p^2 q_4^2\Big)} \\ & - \frac{2\vec{q}^2(1 + \kappa_p)}{(\bar{q}^4 + 4m_e^2 q_4^2) \cdot (\bar{q}^4 + 4m_p^2 q_4^2)} - \frac{(3q_4^2 + 2\bar{q}^2)F_2^2}{4m_p^2 \cdot Q^2 \cdot \Big(Q^4 + 4m_e^2 q_4^2\Big)} \Bigg] \end{aligned} \tag{3.13}$$

$$\begin{aligned} \delta(\mathrm{pol})_p &= \Omega \cdot \left[\frac{9}{8} \int_0^\infty \frac{dQ^2}{Q^2} \left(F_2^2(Q^2) - \frac{16}{9} \int_{\nu_{th}}^\infty \frac{d\nu}{\nu} \beta_1(\theta) G_1(\nu, Q^2) \right) \right. \\ &+ \left. 6 \int_0^\infty \frac{dQ^2}{Q^2} \int_{\nu_{th}}^\infty \frac{d\nu}{m_p} \beta_2(\theta) G_2(\nu, Q^2) \right]. \end{aligned} \tag{3.14}$$

Where

$$\Omega = \frac{\alpha m_e}{(1+\kappa_p)\pi m_p} \approx 0.453 \text{ ppm} \tag{3.15}$$

is a useful pre-factor to remove from the integrals. The functions β_1 and β_2 are,

$$\beta_1(\theta) = 3\theta - 2\theta^2 + 2(\theta - 2)\sqrt{\theta(1+\theta)} \tag{3.16}$$

$$\beta_2(\theta) = 1 + 2\theta - 2\sqrt{\theta(1+\theta)}, \tag{3.17}$$

with $\theta = \nu^2/Q^2$. Finally, G_M and G_E are related to F_1 and F_2 by:

$$G_M(Q^2) = F_1(Q^2) + F_2(Q^2), \tag{3.18}$$

$$G_E(Q^2) = F_1(Q^2) - \frac{Q^2}{4m_p^2} F_2(Q^2). \tag{3.19}$$

The various terms in Eq. (3.13) are in direct correspondence with expressions from Bodwin and Yennie [12] but are calculated by a much more direct route first initiated by Drell and Sullivan [17]. We have included the electron propagator correctly, which is important at the current order of precision. The G_M^2 term corresponds to $\Delta E(\mathrm{VV})$ Eq. (5.28) from Bodwin and Yennie, and the F_2^2 term to $\Delta E(\kappa^2) + \Delta E(\mathrm{No.1})$ and Eqns. (5.31+5.34). The two remaining terms correspond to the Zemach correction plus $\Delta E(\mathrm{VO})$, Eqns. (5.18 + 5.24 + 5.36).

An important point to note is that the F_2^2 and polarizability corrections lack an explicit momentum cutoff. While the terms generated by the elastic form factors all contain a factor $(Q^4 + 4m_p^2 q_4^2)$ in the denominator, the behaviour of the form factor F_2 and dispersion relations in the polarizability are crucial to ensure convergence.

Using the standard dipole parameterization for the elastic form factors, Bodwin and Yennie obtained [12],

$$\delta(\text{one-rigid,B\&Y})_p = -33.50(58 + \textit{unknown}) \text{ ppm.} \tag{3.20}$$

This fortuitously cancels any discrepancy between theory and the residual in Eq. (3.4) when combined with their two loop estimate of $\delta(\text{two-rigid}) \approx 0.46$ ppm. Note however that important systematic sources of error remain and are indicated by the *unknown* in Eq. (3.20). The dipole parameterization is known to overestimate the data by roughly 2% at energies below 1 GeV and there are important corrections to the slope which directly effect the proton charge radius [7]. Incorporating these changes results in a shift on the order of a few ppm because the dominant correction in the $\delta(\text{rigid})$ term is very sensitive to the rms charge radius of the proton. As mentioned in the introduction the current estimate of the $\delta(\text{one-pol})$ term is a 4 ppm bound. There is clearly a need to estimate the hadronic corrections to a greater precision using current data.

Finally, we conclude this section by pointing out that $\delta(\text{one-rigid})$ can be easily evaluated analytically in the point like approximation $G_M \rightarrow 1 + \kappa_p$ and $G_E \rightarrow 1$. The result is,

$$\begin{aligned} \delta(\text{one-rigid}) &= -3\frac{\alpha}{\pi} \cdot \frac{m_e m_p}{m_p^2 - m_e^2} \cdot \ln\left(\frac{m_p}{m_e}\right) \cdot \frac{(4-\kappa_p^2)}{4(1+\kappa_p)} \qquad (3.21) \\ &= -2.01 \text{ ppm.} \qquad (3.22) \end{aligned}$$

The proton's structure makes significant modifications to this result as will be demonstrated in the next section. The interesting feature of this result is that only the anomalous moment squared appears in the correction (the Fermi factor has a factor of $(1 + \kappa_p)$ in the numerator). Higher order calculations in muonium are thus greatly simplified since all terms contributing κ_μ^2 can be dropped to the current order of precision. The complication when calculating higher order corrections in hydrogen is therefore two fold: all terms with anomalous moments contributions must be kept and all such terms in general have a form factor dependence.

3.3 Rigid Contribution Evaluation

The form factors that Bodwin and Yennie used to calculate the rigid part of the recoil are given by the dipole parameterization:

$$G_E(Q^2) = \frac{G_M(Q^2)}{(1+\kappa_p)} = G_D(Q^2) = \left(\frac{\Omega^2}{\Omega^2 + Q^2}\right)^2, \tag{3.23}$$

with $\Omega = 0.843(12)$ GeV. This is equivalent to a charge radius of 0.811 fm. The latest measurement of the charge radius by G.G. Simon et al. [7] yields a charge radius of 0.862(12) fm. This value is consistent with recent Lamb shift experiments [1] probably ruling out the use of a smaller radius. Fig. 3-2 shows the Simon parameterization for G_E and G_M. The fit is to a series of four monopole terms:

$$G_E(Q^2) = \sum_{i=1}^{4} \frac{a_i}{(1 + Q^2/m_i^2)}. \tag{3.24}$$

The parameterization for G_M, also incorporated into the evaluation of the rigid term, is similar. These form factors are then used in Eq. (3.13) in order to calculate the one loop rigid contribution. In many cases by changing variables to angular coordinates it was possible to analytically integrate out everything but the momentum dependence. This was then evaluated numerically using MAPLE. By far the most sensitive integral is the $G_M F_1 - (1 + \kappa_p)$ term which is very sensitive to the charge radius and hence to the slope of the form factors at the $Q^2 = 0$ GeV^2. The net result of this analysis is encapsulated in Table 3.1. The current calculation produces a shift of -1.45 ppm when compared with the work of Bodwin and Yennie. The shift is primarily due to the change in charge radius, however significant modifications to the other terms have also occured at the 0.1 ppm level.

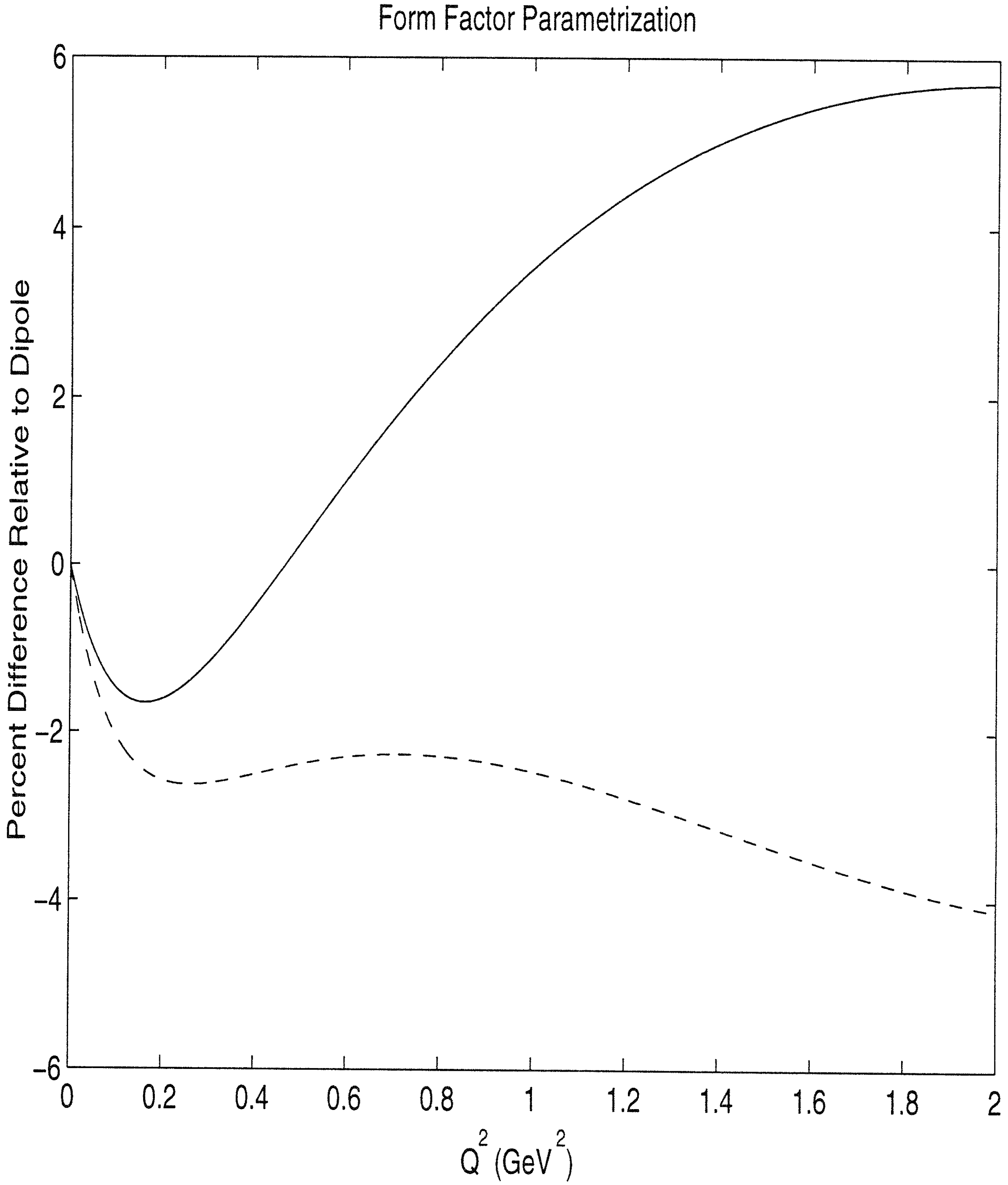

Figure 3-2: The difference ratios of the magnetic and electric form factors $(G_M/(G_D(1+\kappa_p))-1)$ (solid line) and (G_E/G_D-1) (dashed line) with respect to the dipole parameterization of Eq. (3.23).

Term	*Bodwin & Yennie*	*Current Work*
Proton Radius:	0.811 fm	0.862(12) fm
G_M^2	70.05(10)	69.87(10)
F_2^2	-22.44(3)	-22.36(3)
$G_M F_1 - (1+\kappa_p)$	-81.11(57)	-82.46(54)
δ(one-rigid)	-33.50(58)	-34.95(55)

Table 3.1: Comparison between the work of Bodwin and Yennie and the updated δ(one-rigid) contribution. All values are in ppm except for proton radius.

3.4 One Loop Radiative Corrections

The radiative diagrams which affect the two photon exchange calculation are shown in Fig. 3-3. Fortunately, to leading logarithmic order, only the photon polarization insertion need be calculated, as shown in the structureless case by Caswell and Lepage [18]. The leading coefficients of the other diagrams cancel. This can be seen by calculating the leading logarithmic behaviour of the three last diagrams in Fig. 3-3, where the two electron vertex corrections are found to cancel the leading behaviour of the other two diagrams. The dominant behaviour is therefore given by the remaining polarization insertion diagram. As eloquently demonstrated by Landau and Lifshitz [19], the polarization insertion is calculated by replacing the regular photon propagator with,

$$\frac{1}{q^2+i\epsilon} \rightarrow \frac{\alpha}{3\pi}\int_0^1 dx\; x^2(3-x^2)\,\frac{1}{q^2(1-x^2)-4m^2+i\epsilon} \tag{3.25}$$

where m is the mass of the lepton in the loop. We define a function $P(Q^2, m^2)$ given by,

$$\begin{aligned} P(Q^2,m^2) &= \int_0^1 dx\; x^2(3-x^2)\,\frac{Q^2}{Q^2(1-x^2)+4m^2} && (3.26)\\ &= P_L(Q^2,m^2)+P_H(Q^2,m^2) && (3.27)\\ P_L(Q^2,m^2) &= \ln\left(\frac{Q^2+4m^2}{4m^2}\right). && (3.28)\end{aligned}$$

The leading logarithmic behaviour is cleanly separated by writing $x^2(3-x^2) = 2x - x(1-x)^2(2+x)$; the first term leading to the logarithmic term P_L and the second to P_H.

We find that the polarization part of the radiative correction is given by,

$$\delta(\text{one-loop-rad}) = \frac{i\alpha\ |\Psi(0)|^2}{3\pi \mathrm{E_F}} \int \frac{d^4q}{(2\pi)^4} \{T_H^{\mu\nu}\ T^e_{\mu\nu}\} P(-q^2, m_e^2) \frac{-ie^2}{q^2+i\epsilon}\ \frac{-ie^2}{q^2+i\epsilon}, \tag{3.29}$$

where again the braces mean to extract the HFS component. A factor of two has been inserted corresponding to the number of ways the polarization term can be inserted. A complete calculation of radiative corrections to the two photon exchange diagram must also include a term of the following form,

$$\delta(\text{electron-rad}) = \frac{i\alpha\ |\Psi(0)|^2}{2\pi \mathrm{E_F}} \int \frac{d^4q}{(2\pi)^4} \{T_H^{\mu\nu}\ R^e_{\mu\nu}\} \frac{-ie^2}{q^2+i\epsilon}\ \frac{-ie^2}{q^2+i\epsilon}. \tag{3.30}$$

$R^e_{\mu\nu}$ contains the renormalized contributions from the last three diagrams in Fig. 3-3. The net effect is that $S_1^e \rightarrow R_1^e$ picks up terms and $S_2^e \rightarrow R_2^e$ will contain terms proportional to the electrons anomalous moment as a result of vertex corrections. However, the worst singularities will cancel, leaving a correction of the same order as P_H for the photon polarization correction. Thus the leading logarithmic correction is given by,

$$\delta(\text{one-loop-rad}) = \frac{16\alpha m_p^2\Omega}{3\pi^2} \int_0^\infty dq_4 d|\vec{q}|\vec{q}^2 \Big[I + II.A + II.B + III\Big]. \tag{3.31}$$

Where the terms I, $II.A$, $II.B$ and III are given by,

$$I = \frac{3G_M^2 q_4^2 \cdot P_L(Q^2, m_e^2)}{\left(Q^4 + 4m_e^2 q_4^2\right) \cdot \left(Q^4 + 4m_p^2 q_4^2\right)}, \tag{3.32}$$

$$II.A = \frac{2\vec{q}^2\left(G_M F_1 - (1+\kappa_p)\right) \cdot P_L(Q^2, m_e^2)}{\left(Q^4 + 4m_e^2 q_4^2\right) \cdot \left(Q^4 + 4m_p^2 q_4^2\right)},$$

$$II.B = 2\vec{q}^2(1+\kappa_p) \cdot \left(\frac{P_L(Q^2, m_e^2)}{(Q^4 + 4m_e^2 q_4^2) \cdot (Q^4 + 4m_p^2 q_4^2)}\right., \tag{3.33}$$

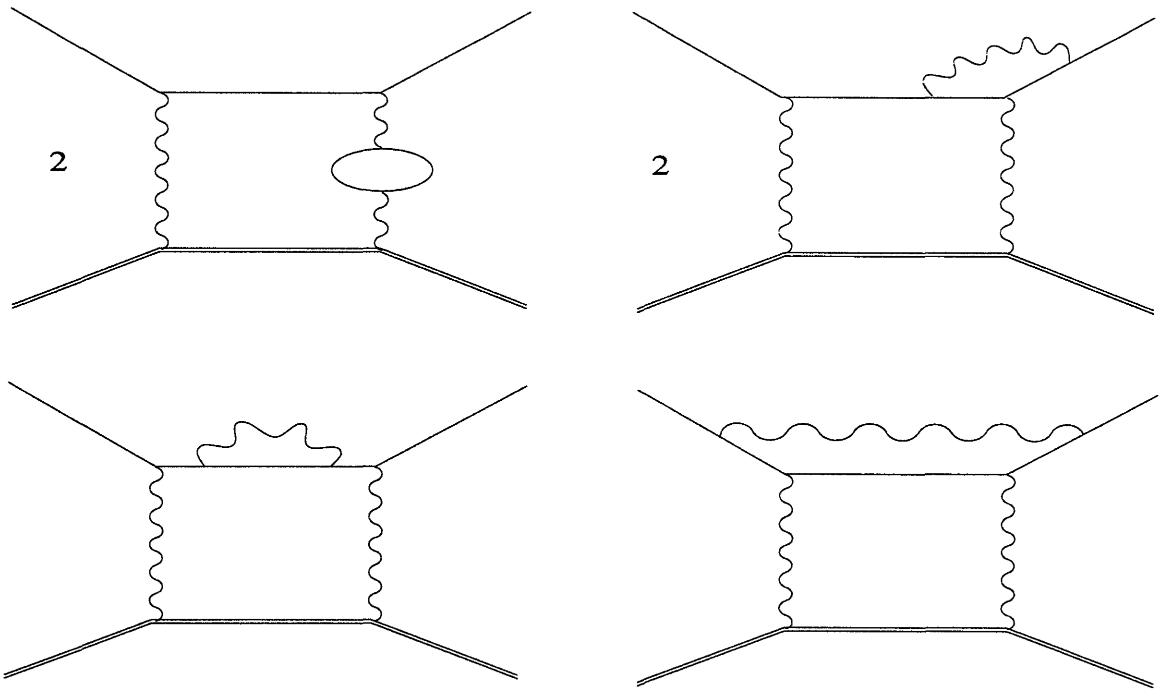

Figure 3-3: The radiative correction diagrams. Missing are the diagrams with crossed photon legs. The diagram in the upper left is the dominant polarization insertion.

$$
- \frac{P_L(\vec{q}^2, m_e^2)}{(\vec{q}^4 + 4m_e^2 q_4^2) \cdot (\vec{q}^4 + 4m_p^2 q_4^2)} \Bigg), \tag{3.34}
$$

$$
III = \frac{-(3q_4^2 + 2\vec{q}^2) F_2^2 \cdot P_L((q_4^2 + \vec{q}^2), m_e^2)}{4m_p^2 \cdot Q^2 \cdot \left(Q^4 + 4m_e^2 q_4^2\right)}. \tag{3.35}
$$

Term II has been broken up into structure dependent and independent terms for ease of numerical analysis. Table 3.2 contains the results of numerically integrating the terms in (3.31). The integration was performed analytically to obtain one dimensional integrals which where then evaluated numerically using the MAPLE program. The

Term	ppm
I	0.502
$II.A$	-0.434
$II.B$	-0.655
III	-0.171
δ(one-loop-rad)	-0.758

Table 3.2: Contributions to the polarization insertion from the terms defined in the text, using the Dipole form factors of Simon et al. All values are in ppm.

total contribution from all the leading terms was found to be -0.758 ppm. The naive estimate for the non leading terms is ≈ 0.1 ppm; nominally the magnitude of the non leading terms should be suppressed by a factor of $\ln(m_p/m_e) \approx 7.6$ from the leading result. Therefore the radiative calculation is consistent with the current QED precision of 0.1 ppm.

3.5 The Polarizability Contribution

The first term of Eq. (3.14) looks highly divergent at low Q^2. That it is not relies on the validity of the Drell-Hearn-Grasimov (DHG) sum rule. The DHG sum rule states that,

$$\int_{\nu_{th}}^{\infty} \frac{d\nu}{\nu} G_1(\nu, 0) = -\frac{F_2^2(0)}{4} = \frac{-\kappa_p^2}{4}. \tag{3.36}$$

Where again, ν_{th} is the pion production threshold. The sum rule follows from applying Low's low energy theorem to the dispersion relation for S_1. An explicit calculation to lowest order reveals that:

$$S_1(\nu, Q^2) = -2F_1\big(F_1 + F_2\big)\left(\frac{1}{2m_p\nu - Q^2 + i\epsilon} - \frac{1}{2m_p\nu + Q^2 + i\epsilon}\right)m_p^2 - F_2^2. \tag{3.37}$$

Therefore there is an implied relationship between $F_2^2(0)$ and the G_1 dispersion integral evaluated at zero energy when Eq. (3.37) is compared with Eq. (3.7). The DHG sum rule in combination with the properties of the β_i functions, insure that the low Q^2 behavior of the integrand is proportional to Q and not $1/Q$ for both dispersive integrals. The weight functions β_1 and β_2 are defined on $0 < \theta < \infty$. They are bounded functions satisfying $-9/4 < \beta_1 < 0$ and $0 < \beta_2 < 1$. The lower limit in both cases corresponds to large θ, which in turn corresponds to the low Q^2 and deep inelastic scattering (DIS) regions. The expression for $\delta(\text{pol})$ in Eq. (3.14) can therefore be decomposed as follows:

$$\delta(\text{pol}) = \delta(\text{pol}, Q < Q_{cut}) + \delta(\text{pol}, Q > Q_{cut}). \tag{3.38}$$

We find ourselves in the strange position of knowing less about the polarizability below the cut than above. This is due to the large number of spin dependent experiments which have been performed recently in a Q^2 range between $2-10$ GeV^2. The majority of experiments in the resonance region have measured unpolarized pion electroproduction cross sections. We analyze this exclusive pion channel data to reconstruct inclusive spin dependent observables under the strong assumption that the one pion channel dominates the low energy behaviour. The one advantage this has over inclusive spin independent measurements is that inclusive data do not currently exist in the resonance region. This resonance parameterization was then used to estimate the low cut contribution to the polarizability. The high cut region was approximated using the DIS expansion. There should be a region between 1 GeV^2 $< Q^2_{cut} <$ 3 GeV^2 where this overlap makes sense as this is typically where resonance behaviour can be understood in terms of higher twist corrections.

There are a number of internal inconsistencies in the available pion electroproduction data. Given a more complete data set it would be interesting to discuss the saturation of $\delta(\text{pol})$ from pion electroproduction; for this reason Appendix B contains details of the parameterization. The Breit-Wigner approach used here has a number of problems which are known to exist at the photoproduction point. Karliner demonstrated that the one pion contributions to the DHG sum rule makes up about 95% of the total sum rule [24]. When decomposed into isospin components, he found that the isovector-isovector part saturates 83% of the DHG sum rule and is quite independent of analysis. The isoscalar-isoscalar term is found to be small and the isoscalar-isovector interference is of the wrong sign and yet accounts for the remaining 10% [23] [24] [25] [26]. Attempts to include non-resonance effects tend to oversaturate the sum rule by up to $10-25\%$. Assuming that these problems persist into the electroproduction region, we concluded that the parameterization was probably good to about 30% overall. Somewhat remarkably if the data is normalized, so that it saturates the DHG sum rule at $Q^2 = 0$, $\delta(\text{pol}, Q < Q_{cut})$ behaves quite well (see Fig 3.4).

The basic picture to keep in mind when trying to understand the Q^2 dependence

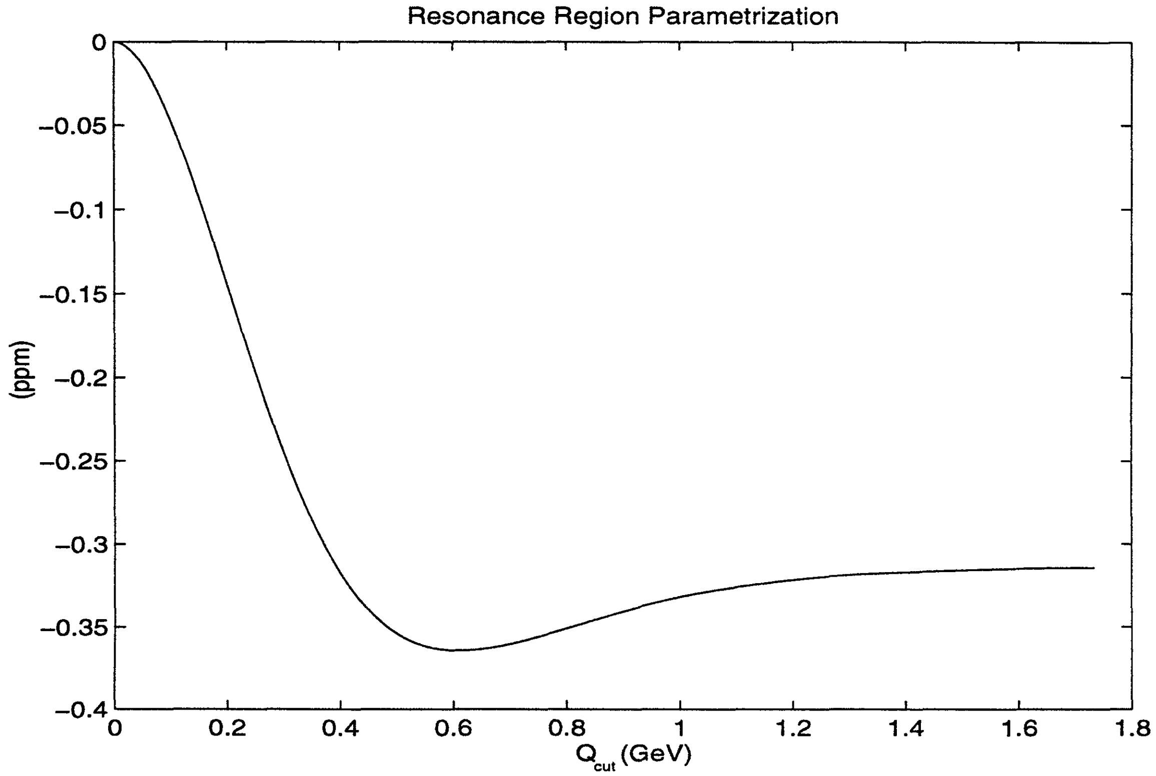

Figure 3-4: The dependence of the Resonance parameterization $\delta(\mathrm{pol}, Q < Q_{cut})$ on Q_{cut}.

of the structure functions is that at low Q^2, the dominant resonances such as the delta couple to the photon through helicity violating transitions, giving G_1 a negative sign. As Q^2 is increased these transitions rapidly drop off. At the same time helicity conserving reactions gain strength and contribute to the non-resonance amplitude. Finally, in the DIS region G_1 becomes predominantly positive. Our analysis below the cut does not include these non-resonance contributions and so $\delta(\mathrm{pol}, Q < Q_{cut})$ is essentially flat for $Q_{cut} > 0.6$ GeV as shown in Fig. 3-4. In contrast, we shall see that the twist expansion for $\delta(\mathrm{pol}, Q > Q_{cut})$ falls appreciably for $Q_{cut} > 1.0$ GeV, indicating the presence of these factors. Our interpretation of this state of affairs is that incoherent behaviour makes important contributions at low Q^2 to $\delta(\mathrm{pol}, Q < Q_{cut})$ and that this information can really only be obtained from detailed experiment. As shown by Fig. 3-4, the observed decay of the resonances with Q^2 is sufficient to neutralize the $F_2^2(Q^2)$ term in Eq. (3.14).

Now consider the polarization correction coming from above the cut: $\delta(\mathrm{pol}, Q >$

Q_{cut}). We deal with the terms coming from G_1 and G_2 separately. The polarization correction for G_1 in the DIS regime is given by,

$$\delta(\mathrm{pol}, G_1, Q > Q_{cut}) = \frac{9}{8}\Omega \int_{Q_{cut}^2}^{\infty} \frac{dQ^2}{Q^2}\left(F_2^2(Q^2) - \frac{32m_p^2}{9Q^2}\int_0^1 g_1(x.Q^2)\beta_1(\theta)dx\right), \quad (3.39)$$

where $g_1(x, Q^2) = \nu/m_p \cdot G_1$ is the deep inelastic scaling function. We have changed our set of integration variables from (ν, Q^2) to (x, Q^2), $x = Q^2/(2m_p\nu)$, $\theta = Q^2/(4m_p^2x^2)$. By expanding around the large θ limit of β_1 an expansion in terms of the moments of g_1 is obtained. Note that for $Q^2 \approx 1$ GeV^2, and $x \approx 1/2$, then $\theta \approx 1$ and the expansion makes sense as $\beta_1(1)/\beta_1(\infty) \approx 0.8$. The twist expansion for the moments is given by,

$$\int_0^1 x^{2n} g_1(x, Q^2)dx = \sum_{\tau=2,4}^{\infty} \frac{\mu_{\tau,2n}}{Q^{(\tau-2)}}, \quad (3.40)$$

where the logarithmic dependence from radiative corrections has been suppressed. Thus $\delta(\mathrm{pol}, G_1)$ above the cut becomes to the relevant order,

$$\delta(\mathrm{pol}, G_1, Q > Q_{cut}) = 9\Omega\left(\int_{Q_{cut}^2}^{\infty} \frac{dQ^2F_2^2}{8 \cdot Q^2} + \frac{m_p^2}{Q_{cut}^2}\cdot\left(\mu_{2,0} + \frac{m_p^2}{Q_{cut}^2}\left(\frac{1}{2}\mu_{4,0} - \frac{5}{9}\mu_{2,2}\right)\right)\right). \quad (3.41)$$

The following estimates have been extracted from spin polarized DIS experiments, $\mu_{2,0} = 0.126(25)$, $\mu_{4,0} = -0.023(15)$ and $\mu_{2,2} = 0.021(10)$ and are used in the analysis (see Chapter Four for explicit details). Fig 3-5 shows the result for this set of parameters. The cusp shown below $Q^2 = 1$ GeV^2 should not be taken seriously, being in a quite nonperturbative domain, but the polarizability correction for a cut larger than ≈ 2 GeV^2 should be accurate.

The $\delta(\mathrm{pol}, G_2, Q > Q_{cut})$ can also be estimated by expanding β_2 in the large θ limit and using the scaling function: $g_2 = (\nu/m_p)^2G_2$ to obtain,

$$\delta(\mathrm{pol}, G_2, Q > Q_{cut}) = \frac{6\Omega m_p^4}{Q_{cut}^4}\left(\Gamma_2 - \frac{4m_p^2}{3Q_{cut}^2}\Gamma_4\right). \quad (3.42)$$

Recent experiments at SLAC by the E143 group have provided estimates for the g_2

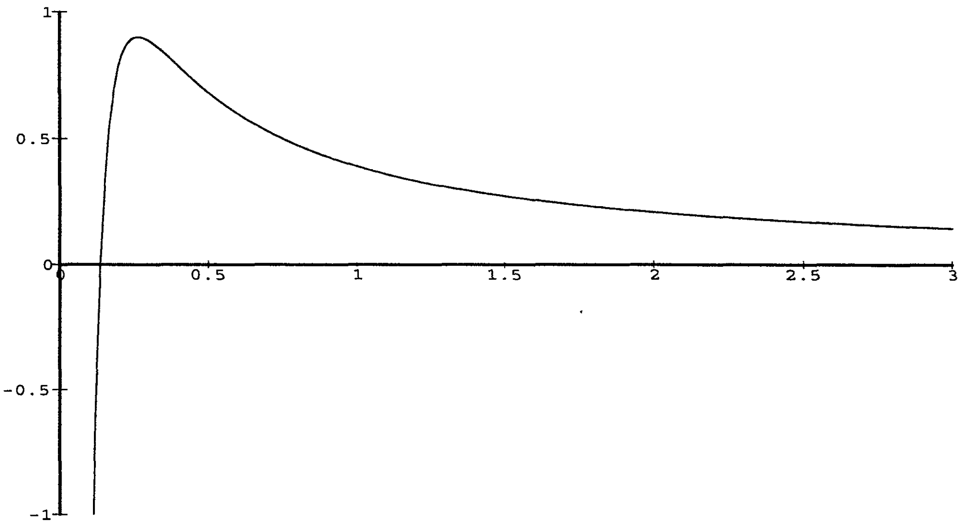

Figure 3-5: The parameterization above the cut, $\delta(\text{pol}, G_1, Q > Q_{cut})$. The horizontal axis is Q^2_{cut} in GeV^2. The vertical axis is in ppm.

moments: $\Gamma_2 = -0.006(2)$ and $\Gamma_4 = -0.002(1)$ at $Q^2 = 5.0$ GeV^2 [27]. We found that the maximum contribution from this set of parameters was on the order of 0.01 ppm and so the G_2 contribution above the cut was neglected.

3.6 Conclusions

The goal of this analysis has been to extract as accurately as possible $\delta(\text{pol})$ from hydrogen hyperfine splitting. Before concluding that the observed discrepancy between theory and experiment is attributable to the polarizability term, we would like to carefully review the various possible sources of uncertainty.

We start with possible QED effects. All the radiative corrections in $f(QED)$ from Eq. (3.3) have been calculated to a precision exceeding 0.1 ppm. Furthermore these results are completely structure independent and are therefore also used in the analysis of muonium. A recent analysis by Kinoshita [11] finds excellent agreement between theory and experiment in muonium hyperfine structure. It is therefore seems improbable that the extraction of the hadronic residual Eq. (3.4) is a significant source of systematic error.

If no further corrections are considered, the data clearly favour a smaller charge radius for the proton. The recent measurement of the $1S$ Lamb shift [1] is however entirely consistent with the 0.862(12) fm radius used in this study. In fact the data prefer a marginally larger radius. Thus it would appear that explaining the discrepancy by changing the charge radius is not a viable option unless there are significant problems with the $1S$ Lamb shift analysis at the 2 ppm level.

The uncalculated subleading radiative contributions could conceivably conspire to produce an effect of the order 0.1 ppm. Likewise the two-loop calculation of Bodwin and Yennie may contain uncalculated effects at the 0.1 ppm level.

Weak interaction effects mediated by Z^0 exchange where discussed in Chapter Two. The standard model estimate of 0.12 ppm has been included in the analysis. While it would interesting if these effects were not as predicted by the standard model, the current estimates say weak effects are only marginally significant at 0.1 ppm precision.

Table 3.3 shows the current theoretical understanding of hydrogen hyperfine splitting. The first row indicates the rms charge radius corresponding to the form factors used in this particular study. The last row shows the residual between hadronic theory and the QED expectation, while the intermediate lines show the magnitude of the effects as discussed in the text. All quantities are in ppm except for the proton charge radius. The consequence of the current work is that the residual between theory and experiment, ignoring polarizability corrections, stands at:

$$\delta(\text{residual}, \text{QED}) = -2.42(56) \text{ ppm}. \tag{3.43}$$

To the best of our knowledge, with uncalculated terms at the level of 0.1 ppm, we can attribute the calculated discrepancy to the polarizability correction,

$$\delta(\text{pol}) \quad = \quad 2.42(58)\text{ppm} \tag{3.44}$$

The error coming almost entirely from the proton elastic form factors. Shortly com-

Term	*Current Analysis* ppm
δ(one-rigid)	-34.95(55)
δ(one-loop-rad)	-0.76
δ(two-loop,B&Y)	0.46
δ(weak)	0.12
δ(net)	-35.13(55)
δ(hadronic, QED)	-32.71(10)
δ(residual, QED)	-2.42(56)

Table 3.3: Summary of the current work in ppm. RMS charge radius: 0.862(12) fm.

parison of this prediction against the spin dependent structure functions G_i, extracted at CEBAF in the relevant low Q^2 kinematic range, will be possible. What is currently required is a proposal to measure the elastic form factors to greater precision. There is considerable need to know the form factors better in the range $0 < Q^2 < m_p^2$. As we have shown, the δ(rigid) is sensitive at the 0.1 ppm level to the $\approx 2\%$ corrections in to the form factors in this range. Increasing the accuracy of the experiment by a factor of five would bring the net error from δ(rigid) down to about 0.1 ppm. The error would then be consistent with the current precision with which the hadronic correction is extracted using QED. Unfortunately the slated CEBAF experiments will not decisively change the uncertainty in the proton charge radius; the form factors will be remeasured but with approximately the same error bars as now.

There are a number of other experiments which would be generally useful. The ingenuity of the atomic physics experimentalists has been steadily increasing the precision of the various fundamental constants. The recent improvement of the electron mass [28] by a factor of ten is a case in point. However, the extraction of the hadronic term in Eq. (3.4) is currently limited by the error in the fine structure constant and to a lesser extent by the magnetic moment of the proton (See appendix D for a table of the relevant constants).

In conclusion, we have extracted from HFS splitting the polarizability contribution and find $\delta(\text{pol}) = 2.42(56)$ ppm. This value is consistent with a 4 ppm bound derived by Gnadig and Kuti [13] using unpolarized data and the pion electroproduction analysis which predicts $\delta(\mathrm{pol}) \approx 0$ ppm but with large uncertainties. The high cut parameterization $\delta(\mathrm{pol}, G_1, Q > Q_{cut})$ behaves in a manner entirely consistent with a positive polarizability. The extracted polarizability provides an interesting independent constraint on the structure functions G_1 and G_2. All known corrections at the 0.1 ppm level have been evaluated for the first time. Comparison of this result with the spin dependent structure function data from CEBAF is eagerly anticipated.

Chapter 4

Deep Inelastic Scattering

This second section of the thesis deals with slightly higher energy and concerns the calculation of twist corrections to the lowest moments of the spin dependent structure functions. After introducing the basic formalism for deep inelastic scattering we discuss the operator product expansion and its application to scaling violations. The scaling violations take the form of logarithmic corrections resulting from perturbative radiative corrections, and higher twist corrections which are important at intermediate Q^2. By way of being an introductory chapter, large quantities of the material presented here can be found in such texts as Muta [31] and Yndurâin [32]. We include a discussion on target mass corrections to the spin dependent structure functions which is not available in the literature.

Fig. 4-1 shows the standard one boson exchange diagram describing lepton scattering on a hadron target. In inclusive scattering,

$$l + H \rightarrow l + W \tag{4.1}$$

where H is the initial hadron and W represents the final state. No particles are detected except for the scattered lepton l. The kinematics are characterized by specifying two of the following kinematic parameters,

$$Q^2 \;=\; -q^2 = -(k - k')^2 \tag{4.2}$$

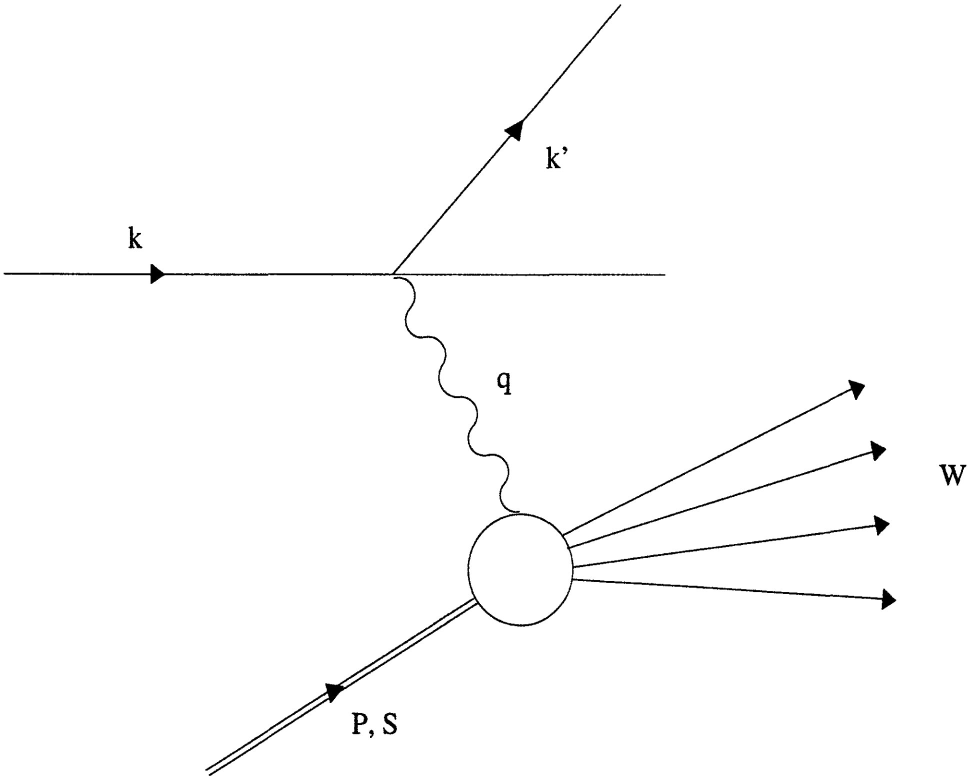

Figure 4-1: Lepton scattering off a hadron target with initial momentum P and spin S, the momentum transfer is given by q.

$$\nu = \frac{P \cdot q}{m_p} \tag{4.3}$$
$$W^2 = (P+q)^2 = m_p^2 + 2m_p\nu - Q^2. \tag{4.4}$$

Here, Q^2 is minus the momentum transfer squared, k and k' are the incident and scattered momenta of the lepton, respectively. Since in this process the interacting virtual boson is space-like, the invariant momentum transfer squared will be negative. The energy transfer is given by ν, with the hadron at rest in the lab frame. W is the four momentum of the debris resulting from the scattering. The spin of the proton is specified by S^μ, with the normalization: $S^2 = -m_p^2$. The mediating boson in this interaction will typically be a photon, but $\gamma - Z_0$ interference and $W^\pm$ interactions can be studied at the expense of greatly reduced cross section. Implicit in this discussion is the assumption that single boson exchange dominates the reaction. Since the electromagnetic coupling is given by the fine structure constant α_{em}, two photon contributions to the cross section will be suppressed by a factor of α_{em}^2, which exceeds the experimental precision of typically a few percent. QED radiative corrections however are essential when analyzing the data. Our primary interest will be in photon mediated scattering and we will hence forth limit our discussion to this case.

The cross section can be factored into a leptonic and hadronic tensor,

$$d\sigma \propto \frac{\alpha^2}{Q^4} L_{\mu\nu} W^{\mu\nu}. \tag{4.5}$$

Where,

$$\begin{aligned} L^{\mu\nu} &= 2k^\mu k^\nu + (k \cdot q) g^{\mu\nu} - k^\mu q^\nu - k^\nu q^\mu + 2i\epsilon^{\mu\nu\alpha\beta} k_\alpha q_\beta, & (4.6)\\ W^{\mu\nu} &= \frac{1}{4\pi} \int d^4\xi e^{i\xi\cdot q} \langle P, S | [J^\mu(\xi), J^\nu(0)] | P, S \rangle. & (4.7) \end{aligned}$$

By considering Lorentz symmetry, gauge invarience, and parity conservation $W^{\mu\nu}$ is restricted to four tensor structures. The only objects available to build such tensors are the vectors P^μ and q^μ; the psuedovector S^μ; the tensor $g^{\mu\nu}$ and psuedotensor $\epsilon^{\mu\nu\alpha\beta}$. There are two symmetric spin-independent structure functions, W_1 and W_2 and two spin-dependent antisymmetric structure functions, G_1 and G_2 which multiply the tensor structures. The conventional parameterization is,

$$\begin{aligned} W^{\{\mu\nu\}}(\nu, Q^2) &= \left(- g^{\mu\nu} + \frac{q^\mu q^\nu}{q^2} \right) W_1(\nu, Q^2) \\ &+ \left(\left(P^\mu - \frac{m_p \nu}{q^2} q^\mu \right) \left(P^\nu - \frac{m_p \nu}{q^2} q^\nu \right) \right) \frac{W_2(\nu, Q^2)}{m_p^2} & (4.8)\\ W^{[\mu\nu]}(\nu, Q^2) &= i\epsilon^{\mu\nu\alpha\beta} q_\alpha \left(S_\beta \frac{G_1(\nu, Q^2)}{m_p^2} + \left((m_p \nu) S_\beta - (S \cdot q) P_\beta \right) \frac{G_2(\nu, Q^2)}{m_p^4} \right), \\ & & (4.9) \end{aligned}$$

where $\{\}$ denotes symmetric and $[\,]$ signifies antisymmetric with respect to the indices. The hadron tensor is given by the sum,

$$W^{\mu\nu} = W^{\{\mu\nu\}} + W^{[\mu\nu]} \tag{4.10}$$

Regarding the kinematic variables Q^2 and ν defined earlier, it was observed by

Bjorken that when $Q^2 \to \infty$ and $\nu \to \infty$ in such a way that

$$x_B = \frac{Q^2}{2m_p\nu} \tag{4.11}$$

is held constant, the data becomes roughly independent of Q^2 and ν, and depends only on x_B. For large Q^2 and ν Bjorken scaling implies that $q_0 - |\vec{q}| \approx x_B m_p + \mathcal{O}(\frac{m_p^2}{\vec{q}})$. Kinematical constraints restrict the range of x_B to lie between zero (completely inelastic) and one (completely elastic scattering). This implies that the important physics for scaling takes place when q is near the light cone. In addition, scaling implies the existence of point-like structure within the hadron, pointed out by Feynman. An analogous phenomena at much lower energy is quasi-elastic scattering on nuclei. The underlying substructure there, consists of protons and neutrons, which compose the nucleus. The nucleons are scattered incoherently when the wavelength of the probe becomes comparable to their characteristic size of $\mathcal{O}$(fm), corresponding to the Impulse approximation picture. The identification of hadronic substructure with valence quarks in the nonrelativistic quark model or the MIT Bag model is therefore heuristic, but the correct picture is more complicated. The scale breaking effects coming from renormalization and the mixing of quark and gluon degrees of freedom need to be taken into account through use of the renormalization group equation. Theory predicts and experiment finds that at large momentum transfer, the quarks only carry about half the momentum of the proton, with the gluon fields responsible for the rest. At lower energies the "bare" quarks seen at higher energies are dressed by clouds of virtual particles and loosely correspond to the valence quark model picture.

The structure functions W_i and G_i as defined by Eqns. (4.8) and (4.9) are dimensionless. This was accomplished by arbitrarily introducing the mass of the hadron m_p to balance dimensions. Since the rest mass of the hadron has nothing to do with the scaling energy ν we should instead define a new set of functions, with ν providing the normalization instead of m_p. These functions should then scale, i.e. become functions of x_B, and depending only weakly on Q^2. This definition leads to

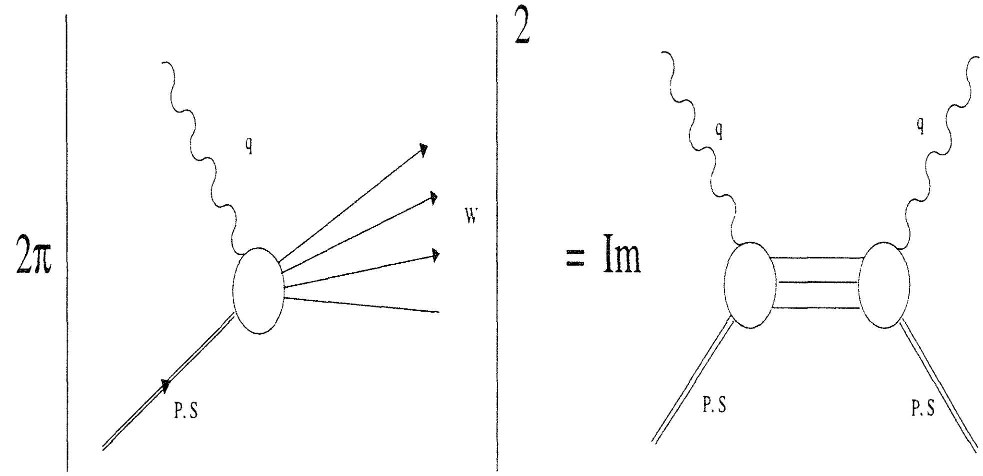

Figure 4-2: A pictorial representation of the optical theorem relating the physical cross section to the imaginary component of the forward Compton amplitude.

the following scaling functions:

$$F_1(x,Q^2) = W_1(\nu,Q^2), \qquad F_2(x,Q^2) = \frac{\nu}{m_p}W_2(\nu,Q^2), \tag{4.12}$$

$$g_1(x,Q^2) = \frac{\nu}{m_p}G_1(\nu,Q^2), \quad g_2(x,Q^2) = \frac{\nu^2}{m_p^2}G_2(\nu,Q^2). \tag{4.13}$$

4.1 Dispersion Theory

A general structure function $B(\nu,Q^2)$ is related by the optical theorem to the corresponding forward Compton amplitude $A(\nu,Q^2)$ as follows,

$$B(\nu,Q^2) = \frac{1}{2\pi}\mathrm{Im}(A(\nu,Q^2)). \tag{4.14}$$

Fig. 4-2 graphically represents this relationship. The analytic structure of the forward Compton amplitudes can then be used to relate physical scattering information along the branch cuts to moments of the structure functions. For a generic analytic

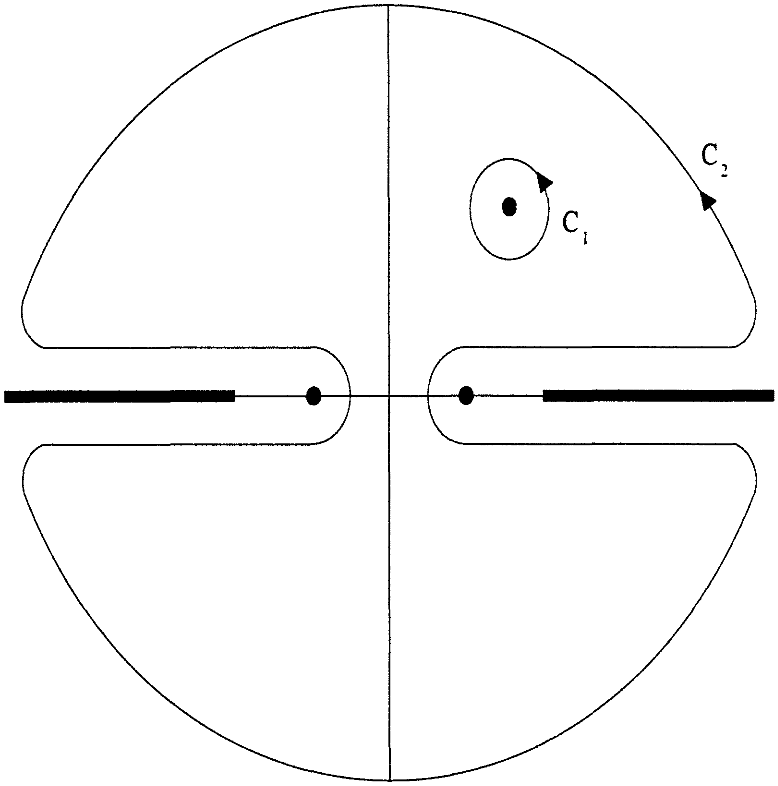

Figure 4-3: The complex ν plane, showing poles, branch cuts and the two contour integrals C_1 and C_2.

amplitude $A(\nu)$ real, except along the branch cuts,

$$\begin{aligned} A(\nu) &= \frac{1}{2\pi i}\oint_{C_1} \frac{A(\nu')d\nu'}{\nu'-\nu} && (4.15)\\ &= \frac{1}{2\pi i}\oint_{C_2} \frac{A(\nu')d\nu'}{\nu'-\nu}, && (4.16)\end{aligned}$$

where the Q^2 dependence has been suppressed and C_1 and C_2 are the contours outlined in Fig. 4-3. The analytic structure provides two further constraints: the first is that the reality of $A(\nu)$ on a region of the $\Re(\nu)$ axis implies a reflection property discussed initially by H.A. Schwarz, and secondly the covariant formulation of the Compton amplitude requires crossing symmetry to hold. These two powerful analytic constraints,

$$\begin{aligned} A(\nu^*) &= A^*(\nu) && (4.17)\\ A(\nu)_\pm &= \pm A(-\nu)_\pm, && (4.18)\end{aligned}$$

make further progress possible with Eq. (4.16). Specifically Eq. (4.9) tells us that G_1 is even and G_2 is odd under the transformation $\{\mu \leftrightarrow \nu, q \rightarrow -q\}$ corresponding to crossing symmetry in Eq. (4.18). Taking the contour C_2 infinitesimally close to the branch cuts quickly leads to two possible dispersion relations,

$$\begin{aligned} A(\nu)_+ &= P_+ + 4\int_{\nu_{th}}^{\infty} \frac{d\nu'\nu'\ B(\nu')_+}{\nu'^2 - \nu^2} && (4.19) \\ A(\nu)_- &= P_- + 4\int_{\nu_{th}}^{\infty} \frac{d\nu'\nu\ B(\nu')_-}{\nu'^2 - \nu^2}, && (4.20) \end{aligned}$$

where $P_\pm$ are pole terms specified by the situation under study. The real functions $B_\pm$ are defined by,

$$4\pi i B(\nu)_\pm = \lim_{\epsilon\to 0}\Big(A(\nu + i\epsilon)_\pm - A(\nu - i\epsilon)_\pm\Big), \qquad (4.21)$$

where the right hand side is twice the imaginary part of the forward Compton amplitude across the branch cut. Changing variables by substituting $x = \frac{Q^2}{2m_p\nu}$ at fixed Q^2 leads to the analytic expansion in $\frac{1}{x}$,

$$\begin{aligned} A(x)_+ &= 4\sum_{n=1}^{\infty}\int_0^{1^+} dx' B_+(x')\frac{x'^{2n-1}}{x^{2n}}, && (4.22) \\ A(x)_- &= 4\sum_{n=0}^{\infty}\int_0^{1^+} dx' B_-(x')\frac{x'^{2n}}{x^{2n+1}}. && (4.23) \end{aligned}$$

The pole terms coming from elastic scattering are located a $x = 1$, the integration limit $x \rightarrow 1^+$ includes the elastic delta function contribution. Typically the lowest few moments ($n < 8$) can be extracted from experiment and compared with the operator product expansion.

4.2 Operator Product Expansion and Twist

Knowing that the dominant physics at high energy takes place near the light cone leads naturally to the operator product expansion. The technique systematically expands an operator about the light cone and takes into account the dominant light cone singularities in an orderly way. This technique was developed originally by Wilson and has proven generally useful in the analysis of high energy processes.

The primary observation is the existence of two scales in the problem. The first scale is characterized by the momentum transfer Q^2 used in the experiment. This scale should be in a regime where perturbation theory is applicable. A second scale μ^2, is chosen to be the renormalization scale. The bilocal matrix elements of the current can be written as an infinite sum of local operators, where the high energy behaviour has been separated from the low energy. An infinite tower of Lorentz contractions links the two factors,

$$T^{\mu\nu}(Q^2,x) = \sum_{i,n} \tilde{C}_i\Big(Q^2/\mu^2, \alpha_S(Q^2)\Big)^{\mu\nu\mu_1\cdots\mu_n} O_i(P,S,\mu^2)_{\mu_1\ldots\mu_n}. \tag{4.24}$$

$\tilde{C}_i$ contains the hard or perturbative aspects of the operator. $\tilde{C}_i$ is calculated using QCD perturbation theory and thus depends on the strong coupling constant α_S at the renormalization scale of the calculation. $\tilde{C}_i$ can be further expanded into a dimensionless coefficient function C_i and a tensor structure built from q^μ; the only quantity available containing hard momentum. Since $T^{\mu\nu}$ and C_i are dimensionless, the tensor structure determines the mass dimension of the low energy part. O_i are the soft matrix elements and depend on the renormalization scale of the calculation μ^2 and are built out of P and S.

The actual physics however cannot depend on μ^2, and this leads directly to the renormalization group equation:

$$\left(\delta_{ij}\Big(\mu\frac{\partial}{\partial\mu} + \beta(g)g\frac{\partial}{\partial g}\Big) - \gamma_{ij}\right)C_i\Big(Q^2/\mu^2, \alpha_S(Q^2)\Big) = 0. \tag{4.25}$$

Here $\beta(g)$ depends on the details of the theory and determines the evolution of the coupling constant. Gross and Wilczek [35] were the first to notice that the β function was negative for non abelian field theories like QCD. The implication is that the strong coupling constant tends to zero at large energies, leading to the prediction of asymptotic freedom at high energies since,

$$\frac{\partial g^2}{\partial t} = g\beta(g), \tag{4.26}$$

where the strong coupling constant is given by $\alpha_s = g^2/(4\pi)$ and $t = \ln(Q^2/\mu^2)$. The anomalous dimension matrix γ_{ij} is given by

$$\gamma_{ij} = -\left(\frac{\mu}{Z}\frac{\partial Z}{\partial \mu}\right)_{ij}, \tag{4.27}$$

Where Z_{ij} is obtained by renormalizing the bare operators which are μ^2 independent,

$$O_i^R(\mu^2) = Z_{ij}(\mu^2) O_j^B \tag{4.28}$$

The actual method of solving the renormalization group is involved and we relegate the details to the excellent review article by A. Buras [34]. The net effect will be that the evolution of the operator with Q^2 will acquire a logarithmic dependence. In Chapter Six we will examine this evolution for the spin independent structure function F_2, until then we put aside the radiative corrections. We now consider another important class of corrections called higher twists.

The twist of an operator is defined formally as the difference between the total mass dimension D_f of the soft operator, and the operator's spin D_s. The operator's mass dimension is easily inferred from the Lagrangian of the theory while the spin is obtained by analyzing the symmetry of the Lorentz indices of the operator. An n index tensor can generally be decomposed (Schwinger [33]) into a hierarchy of spins, the highest spin being n. This tower of spins orders the contributions of the operator at large Q^2, with the leading term coming from the highest spin component. Since the highest spin cannot exceed the number of indices in the operator, it is quickly noticed that the lowest possible twist is 2. The twist specifies the leading $1/Q^2$ behaviour of the operator as we will now explain. The overall mass dimension of $T^{\mu\nu}$ is zero, therefore the mass dimension of the hard part must balance the soft and is given by $-D_f$. The hard part goes like Q^{-D_f} for purely dimensional reasons. The soft part

Matrix Element	Mass	Spin	Twist
$\langle P,S\vert\bar{\Psi}\gamma^{\mu}\Psi\vert P,S\rangle$	3	1	2
$\langle P,S\vert\bar{\Psi}\gamma^{\mu}\gamma_5\Psi\vert P,S\rangle$	3	1	2
$\langle P,S\vert\bar{\Psi}\gamma^{\mu}\tilde{F}^{\mu_1\mu_2}\Psi\vert P,S\rangle$	5	2,1	3,4
$\langle P,S\vert\bar{\Psi}\gamma^{\mu}\gamma_5 iD^{\mu_1}iD^{\mu_2}\Psi\vert P,S\rangle$	5	3,2,1	2,3,4

Table 4.1: Mass dimensions and twists of various soft matrix elements.

however contains tensors built from P^{μ} and S^{μ}. When the operator's indices are contracted with the hard part, factors of $m_p\nu$ are generated. Each $2m_p\nu/Q^2 = 1/x$ removes in the scaling limit one power of Q from the denominator. In this way one sees that the highest spin component will make the largest contribution in the scaling limit.

Table 4.1 contains a few representative matrix elements and their possible twists. The spin decomposition can be selected by choosing a particular symmetry of the indices. For example, in the last term in Table 4.1, if the indices are completely symmetrized the spin is three, mixed symmetric spin two. The completely antisymmetric component has spin one. Thus this matrix element makes contributions at twist-two, three, and four.

4.3 Target Mass Corrections

One form of $1/Q^2$ correction which can be simply understood are target mass corrections. The leading twist-two calculation, does not depend on the mass scale of the initial hadron due to the scale invariance of the underlying QCD theory. Target mass corrections restore the mass scale in a systematic way. Consider the lowest order forward Compton diagram for parton scattering shown in Fig. 4-4. Since the photon probe can only couple with electric charge, this diagram measures the distribution of charged partons or quarks within the hadron. Since the momentum transfer q is much larger than the hadronic momentum scale, the factorization discussed earlier is clear: the top parts of the diagram containing momenta of $\mathcal{O}(q)$ represents the hard

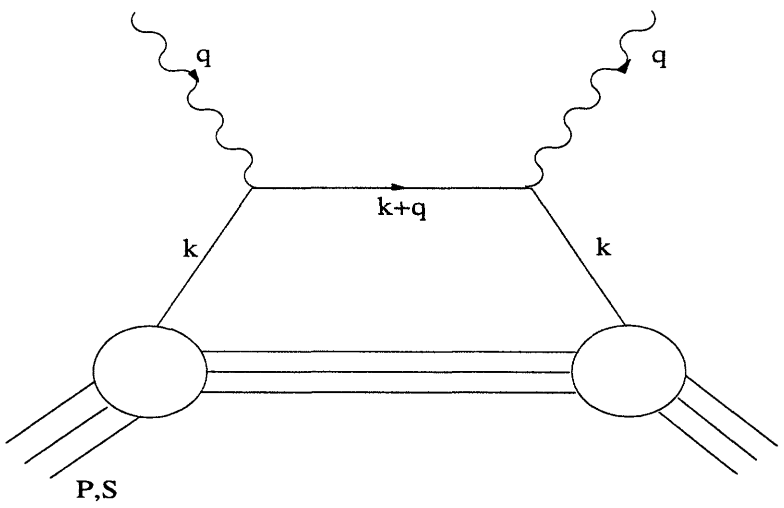

Figure 4-4: Lowest order forward Compton, parton diagram. k is the momentum fraction of the parton, not shown is the crossing diagram.

process, while the bottom part contains the soft dynamics with momenta $\mathcal{O}(P)$. Selecting explicitly the spin dependent antisymmetric component for a particular quark field $\Psi = u, d, \cdots$ we find,

$$\begin{aligned} T^{[\mu\nu]} &= i \int d^4\xi \int \frac{d^4k e^{i\xi\cdot k}}{(2\pi)^4} \langle P, S|\bar{\Psi}(0) \left(\frac{\epsilon^{\mu\nu\alpha\beta}(k_\alpha + q_\alpha)\gamma_5\gamma_\beta}{q^2 + 2k \cdot q} \right. && (4.29) \\ &+ \left. \{q \to -q, \mu \leftrightarrow \nu\} \right) \Psi(\xi)|P, S\rangle && (4.30) \end{aligned}$$

Expanding the denominators followed by a series of integration by parts eliminates the k dependence leaving the following antisymmetric local expression,

$$T^{[\mu\nu]} = i\epsilon^{\mu\nu\alpha\beta} q_\alpha \sum_{n=0}^{\infty} \left(\frac{2}{Q^2} \right)^{2n+1} q^{\mu_1} \cdots q^{\mu_{2n}} \langle P, S|\bar{\Psi}(0)\gamma_\beta\gamma_5 \, iD_{\mu_1} \cdots iD_{\mu_{2n}} \Psi(0)|P, S\rangle \tag{4.31}$$

We would now like to systematically extract from this expression components in order of their significance. Each term in Eq. (4.31) can be decomposed into objects with definite spin. As discussed previously the dominant contribution will come from the highest spin structure. We therefore need to construct symmetric, traceless tensors with $2n+1$ indices to extract the leading twist-two component. The only quantities available are the hadron momentum P^μ and its spin S^μ. S^μ must appear exactly once or not at all due to the linear dependence in $W^{\mu\nu}$ and, since the antisymmetric component currently under analysis contains the axial current

$$\bar{\Psi}\gamma_\mu\gamma_5\Psi = 2S_\mu, \tag{4.32}$$

every term must contain a spin factor. The combinatorics which insure the symmetrization and traceless condition are tedious, and we show only a representative number of intermediate steps.

$$T^{[\mu\nu]} = i\epsilon^{\mu\nu\alpha\beta}q_\alpha \sum_{n=0}^{\infty}\left(\frac{2}{Q^2}\right)^{2n+1} q^{\mu_1}\cdots q^{\mu_{2n}} \sum_{j=0}^{n}\frac{(-1)^j\ (2n-j+1)!}{2^j\ (2n+1)!}a_{2n}\Pi^{2n,j}_{\beta\mu_1\cdots\mu_{2n}} \tag{4.33}$$

Where

$$\begin{aligned}
\Pi^{2n,j}_{\mu_1\cdots\mu_{2n+1}} &= \sum_{\{i_{2n+1}\}}\left(g_{\mu_{i_1}\mu_{i_2}}\cdots g_{\mu_{i_{2j-1}}\mu_{i_{2j}}}\mathcal{L}_{\alpha_1\alpha_1\cdots\alpha_j\alpha_j\ \mu_{i_{2j+1}}\cdots\mu_{i_{2n+1}}}\right) && (4.34)\\
\mathcal{L}^{\mu_1\cdots\mu_{2n+1}} &= \left(\frac{S^{\mu_1}P^{\mu_2}..P^{\mu_{2n+1}} + P^{\mu_1}S^{\mu_2}..P^{\mu_{2n+1}} + +P^{\mu_1}..P^{\mu_{2n}}S^{\mu_{2n+1}}}{2n+1}\right) && (4.35)
\end{aligned}$$

and the $a_{2n}(\mu^2)$ are defined by,

$$a_{2n}\mathcal{L}_{\{\beta\mu_1\cdots\mu_{2n}\}} = \langle P,S|\bar{\Psi}\gamma_{\{\beta}\gamma_5 iD_{\mu_1}\cdots iD_{\mu_{2n}\}}\Psi|P,S\rangle. \tag{4.36}$$

The $a_{2n}(\mu^2)$ coefficient is the expectation value of the soft matrix element and depends on the renormalization scale as discussed earlier. The $j=0$ term reduces to Eq. (4.31) if the symmetry in $\mathcal{L}$ is ignored. The higher j terms enforce the traceless condition.

Utilizing the symmetry of Π allows the evaluation of Eq. (4.33). We find that the complete set of twist-two corrections derived from Fig. 4-2 for S_1 and S_2 are given after a change of variables in the double sum by,

$$\begin{aligned}
S_1(x,Q^2) &= \frac{2m_p^2}{Q^2}\sum_{n=0}^{\infty}\sum_{j=0}^{\infty}\left(\frac{m_p^2}{Q^2}\right)^j\frac{(2n+j+1)!\ (2n+1)}{(2n+2j+1)^2\ (2n)!j!}\frac{a_{2(n+j)}}{x^{2n}} && (4.37)\\
S_2(x,Q^2) &= -\frac{4m_p^4}{Q^4}\sum_{n=1}^{\infty}\sum_{j=0}^{\infty}\left(\frac{m_p^2}{Q^2}\right)^j\frac{(2n+j+1)!}{(2n+2j+1)^2\ (2n-1)!j!}\frac{a_{2(n+j)}}{x^{2n-1}}. && (4.38)
\end{aligned}$$

The powers of x in the denominator appear by combined factors of $P\cdot q = m_p\nu$.

These result from contracting q^{μ_i} against the P^{μ_i} within Π, with leftover powers of $2/Q^2$ as discussed in the last section. The powers of m_p^2 in the numerator arise from contracting powers of P^μ against themselves, a consequence of imposing the traceless condition.

Applying dispersion theory to S_1 and S_2 as done previously for the generic amplitudes and identifying powers of $1/x$, leads ultimately to a relationship between moments of the spin dependent scaling functions and the leading twist matrix elements:

$$\int_0^1 dx x^{2n} g_1(x,Q^2)|_{T_2} = \frac{1}{4}\sum_{j=0}^{\infty}\left(\frac{m_p^2}{Q^2}\right)^j \frac{(2n+j+1)!(2n+1)}{(2n+2j+1)^2\,(2n)!\,j!} a_{2(n+j)} \tag{4.39}$$

$$\int_0^1 dx x^{2n} g_2(x,Q^2)|_{T_2} = -\frac{1}{4}\sum_{j=0}^{\infty}\left(\frac{m_p^2}{Q^2}\right)^j \frac{(2n+j+1)!}{(2n+2j+1)^2\,(2n-1)!\,j!} a_{2(n+j)}. \tag{4.40}$$

The first sum is valid for $n = 0, 1, \cdots$ while the second is only valid for $n = 1, 2, \cdots$. The actual derivation has nothing to say about the lowest moment of g_2 but there are arguments on the grounds of rotational invariance that $\int_0^1 dx g_2(x) = 0$. This relation is called the Burkhardt-Cottingham sum rule.

The twist-three target mass contribution can be extracted by analyzing indices with mixed symmetry, thus reducing the spin by one unit.

$$d_{2n}\mathcal{M}_{[\beta\{\mu_1]\mu_2\cdots\mu_{2n}\}} = \langle P,S|\bar{\Psi}\gamma_{[\beta}\gamma_5 iD_{\{\mu_1]}iD_{\mu_2}\cdots iD_{\mu_{2n}\}}\Psi|P,S\rangle \tag{4.41}$$

Where $\mathcal{M}$ is antisymmetrized in the first two indices and then symmetrized in all except the first. The clearest way to analyze this term is to note that,

$$\mathcal{M}^{\beta\mu_1\cdots\mu_{2n}} = S^\beta P^{\mu_1}\ldots P^{\mu_{2n}} - \mathcal{L}^{\beta\mu_1\cdots\mu_{2n}}. \tag{4.42}$$

The previous twist-two analysis then shows that the S_1 contribution is zero, and only S_2 receives a twist-three correction with sign opposite to the leading twist contribution. The total twist-two and three target mass corrections are found to be,

$$\int_0^1 dx x^{2n} g_1(x,Q^2)|_{T_{2\&3}} = \frac{1}{4}\sum_{j=0}^{\infty}\left(\frac{m_p^2}{Q^2}\right)^j \frac{(2n+j+1)!(2n+1)}{(2n+2j+1)^2\,(2n)!\,j!} a_{2(n+j)} \tag{4.43}$$

$$\int_0^1 dx x^{2n} g_2(x,Q^2)|_{T_{2\&3}} = \frac{1}{4}\sum_{j=0}^{\infty}\left(\frac{m_p^2}{Q^2}\right)^j \frac{(2n+j+1)!}{(2n+2j+1)^2\,(2n-1)!\,j!}\Big(d_{2(n+j)} - a_{2(n+j)}\Big) \tag{4.44}$$

These expressions will be useful, in Chapter Five, where we discuss twist-four corrections to the first moment of G_1. At twist-four other operators, in particular gluonic fields such as the third term in Table 4.1 must be taken into account along with the target mass corrections. The complexity grows as the number of matrix elements at a given twist increases rapidly. As will be seen however, at the level of twist-four, progress can be made by using the QCD equations of motion.

4.4 Bjorken and Ellis-Jaffe Sum Rules

The target mass corrections derived in the previous section contain the Bjorken sum rule [36] as their leading term. For all that follows we systematically neglect radiative corrections which we signify by not indicating any Q^2 dependence. Consider the first moment of g_1. Taking $j = 0$ in Eq. (4.43) then the difference between the proton and neutron moments is,

$$\int_0^1 dx(g_1^p(x) - g_1^n(x)) = \frac{1}{4}(a_0^p - a_0^n) \tag{4.45}$$

The superscripts p and n refer to proton and neutron respectively and imply that we have added a charge matrix to the results calculated in the previous section and summed over the appropriate quark configurations. Since a_0 is related directly to the axial current, Bjorken found

$$\int_0^1 dx(g_1^p(x) - g_1^n(x)) = \frac{1}{6}(g_A^u - g_A^d) \tag{4.46}$$

$$= \frac{1}{6}(F+D) = \frac{g_A}{6} \qquad (4.47)$$

where g_A^i are the axial couplings for the particular quark current in question and $g_A = 1.257$ is the axial current. F and D are $SU(3)$ matrix elements which can be measured by studying semileptonic decays. By making assumptions about the flavour structure of the quark distributions, Ellis and Jaffe [37] separated the Bjorken sum rule into a proton and neutron dependent piece. This separation was made possible by assuming that contributions from the strange quark were negligible. Under this assumption they found,

$$\begin{aligned} \int_0^1 dx g_1^p(x) &= \frac{1}{18}(9F-D) && (4.48) \\ \int_0^1 dx g_1^n(x) &= \frac{1}{18}(6F-4D). && (4.49) \end{aligned}$$

Experiments at EMC found that $\int_0^1 dx g_1^p(x) = 0.126(25)$, whereas the Ellis-Jaffe sum rule predicts a larger value ≈ 0.175. This lead to much discussion in the literature and has come to be known as the "spin crisis". Experiments to measure the more fundamental Bjorken sum rule have therefore become an important concern. These experiments are performed using bound neutrons in light nuclei such as deuterium and helium three, which complicate the analysis. The current situation however, seems to indicate that the Bjorken sum rule is satisfied when finite Q^2 effects are taken into account. The next chapter addresses the twist-four corrections to this important sum rule and proposes a model for the behaviour of the proton's first moment from low to high Q^2.

Chapter 5

Q^2 Evolution of the G_1 Sum Rule

Recently, polarized deep-inelastic scattering has proven to be an excellent tool for studying the spin structure physics of the nucleon [38, 39, 40]. Supplemented with the operator product expansion analysis in Quantum Chromodynamics (QCD), experimental data at high-energy provides a direct measurement of the matrix elements of spin-dependent operators in the nucleon. A much discussed example in the current literature is the axial charge, or the forward matrix element of axial current, whose measurement by the EMC collaboration casts doubt on our traditional understanding of the proton's spin structure [38].

A closely related question is can one learn anything about the nucleon's spin structure from electro-production experiments away from the deep-inelastic limit? In particular, what insight do the spin structure functions G_1 and G_2 provide at low and moderate Q^2? Not long ago, Anselmino et al. [41] pointed out that at the real photon point ($Q^2 = 0$), the first moment of G_1 (called the sum rule in the following text) is related, via the celebrated Drell-Hearn-Gerasimov (DHG) sum rule [42], to the anomalous magnetic moment of the nucleon, and thus the physics of the G_1 structure function again appears simple in the $Q^2 \to 0$ limit. Together with knowledge from the deep-inelastic limit, the authors in Ref. [41] constructed a model for the sum rule at all Q^2. This has motivated a number of proposals to measure G_1 and G_2 at low energy [43, 58].

In Ref. [45], Ji pointed out that the analysis made in Ref. [41] excluded the nucleon's elastic contribution to the moment, which in the $Q^2 \to 0$ limit dominates the entire inelastic contribution calculated from the DHG sum rule. He argued that the moment has to include this contribution if it is to be analyzed in twist expansion in the deep-inelastic limit and its experimental measurement is to be used to extract the matrix elements of higher-twist operators.

In this Chapter we study the Q^2 variation of the sum rule by exploring the physics of the $Q^2 \to 0$ and $Q^2 \to \infty$ limits. In the first limit, we rely on the low energy result derived in Ref. [45], to calculate the exact value and the first derivative of the sum rule at $Q^2 = 0$. In the second limit, we use a twist expansion appropriate for the deep inelastic region, focusing on the $1/Q^2$ correction term. The matrix elements of higher twist operators are related to moments of the quark distributions functions $g_{if}(x)$ ($i = 1, T, 3$ and $f = u, d, s...$) through a novel use of the QCD equations of motion, which are in turn evaluated in the MIT bag model. As an application, we discuss the correction of higher twists to the Bjorken sum rule in the deep inelastic limit. Having obtained analytical results valid for the low and high ranges of Q^2, we construct a simple parameterization to smoothly interpolate both limits, which should be checked experimentally.

To begin we consider the following fixed-mass sum rule,

$$\Gamma(Q^2) = \frac{Q^2}{2M^2}\int_{Q^2/2}^{\infty} G_1(\nu, Q^2)\frac{d\nu}{\nu}, \tag{5.1}$$

where $G_1(\nu, Q^2)$ is one of the nucleon's spin dependent structure functions in the nucleon tensor,

$$W^A_{\mu\nu} = -i\epsilon_{\mu\nu\alpha\beta}q^\alpha\big[S^\beta\frac{G_1}{M^2} + \frac{G_2}{M^4}(\nu S^\beta - P^\beta(S\cdot q))\big]. \tag{5.2}$$

The lower integration limit in Eq. (5.1) implies the elastic contribution to G_1 is also included. Here P and S are the nucleon's momentum and polarization, q is the virtual photon momentum, M is the nucleon mass, $\nu = P\cdot q$ and $Q^2 = -q^2$ ($\epsilon^{0123} = 1$). In deep-inelastic limit, one defines scaling functions $g_1(x, Q^2) = \nu/M^2 G_1$

and $g_2(x, Q^2) = (\nu/M^2)^2 G_2$. The sum rule then becomes,

$$\Gamma(Q^2) = \int_0^1 g_1(x, Q^2) dx, \tag{5.3}$$

which is just the first moment of the scaling function.

Let us first consider the small Q^2 behavior of the sum rule. Introduce a spin-dependent virtual-photon Compton amplitude $S_1(\nu, Q^2)$ whose imaginary part is proportional to G_1, and write down the unsubtracted dispersion relation,

$$S_1(\nu, Q^2) = 4 \int_{Q^2/2}^{\infty} \frac{\nu' d\nu'}{\nu'^2 - \nu^2} G_1(\nu', Q^2). \tag{5.4}$$

Through this, we relate the sum rule to the Compton amplitude at $\nu = 0$,

$$\Gamma(Q^2) = \frac{Q^2}{8M^2} S_1(0, Q^2). \tag{5.5}$$

At small ν and Q^2, the dominant contribution to S_1 comes from the nucleon pole diagrams [45],

$$S_1^{\text{pole}}(\nu, Q^2) = -2M^2 F_1(F_1 + F_2)[\frac{1}{2\nu - Q^2} - \frac{1}{2\nu + Q^2}] - F_2^2, \tag{5.6}$$

where F_1 and F_2 are the Dirac and Pauli form factors of the nucleon. From this, we obtain for $Q^2 \to 0$,

$$\Gamma(Q^2) = \frac{1}{2} F_1(F_1 + F_2) - \frac{1}{8M^2} F_2^2 Q^2. \tag{5.7}$$

This result can be shown to be accurate up to the order of Q^2 in the small Q^2 region by *explicitly* evaluating Eq. (5.1): The elastic contribution to G_1 is proportional to $\delta(2\nu - Q^2)$, producing the first term in Eq. (5.7); the integral over inelastic contributions is just the DHG sum rule in the limit of $Q^2 \to 0$ and the second term in Eq. (5.7) reproduces this in the same limit.

The elastic contribution vanishes identically at $Q^2 = 0$ because of energy-momentum conservation, and the DHG sum rule indicates $\Gamma(0) = 0$. Thus, due to the elastic contribution, $\Gamma(Q^2)$ is non-analytic around $Q^2 = 0$, i.e.,

$$\Gamma(Q^2 = 0) \neq \Gamma(Q^2 \to 0). \tag{5.8}$$

To remedy this, one can take two approaches: The first approach subtracts away the elastic contribution from the sum rule for $Q^2 \neq 0$. The new sum, $\bar{\Gamma}(Q^2) = \Gamma(Q^2) - 1/2F_1(F_1 + F_2))$, is a smooth extension of the DHG sum rule to virtual-photon scattering. The approach we take in this chapter is to redefine Γ at $Q^2 = 0$,

$$\Gamma(Q^2 = 0) \equiv \Gamma(Q^2 \to 0). \tag{5.9}$$

This approach ensures that the sum rule at low Q^2 can be treated with the twist expansion that we will discuss below. The expansion is for moments of the g_1 structure function which include the integration limit $x = 1$, where the elastic contribution resides.

Since Eq. (5.7) is accurate up to the order of Q^2, we can determine $\Gamma(Q^2)$ and its first derivative in $Q^2 \to 0$ limit,

$$\begin{aligned}
\Gamma^p(0) &= 1.396, \\
\Gamma^n(0) &= 0, \\
\frac{d\Gamma^p(Q^2)}{dQ^2}|_{Q^2=0} &= -8.631\text{GeV}^{-2}, \\
\frac{d\Gamma^n(Q^2)}{dQ^2}|_{Q^2=0} &= -0.479\text{GeV}^{-2},
\end{aligned} \tag{5.10}$$

where p, n refer to proton or neutron and the squares of the proton and neutron charge radii $\langle r_p^2 \rangle_{\text{c.r.}} = (0.862\ \text{fm})^2$ and $\langle r_n^2 \rangle_{\text{c.r.}} = -(0.342\ \text{fm})^2$ have been used. The initial slope of $\Gamma^p(Q^2)$ is primarily determined by the elastic contribution as the inelastic contribution, $-\kappa_p^2/8M^2 = -0.455\text{GeV}^{-2}$, is only about 5% of the total. Therefore, one expects that for small Q^2, $\Gamma^p(Q^2)$ is mainly given by the elastic contribution. In contrast, due to a numerical coincidence, the elastic part of $\Gamma^n(Q^2)$ is negligible compared with the inelastic part.

In the limit of large Q^2 ($Q^2 \gg \Lambda^2_{\rm QCD}$), $\Gamma(Q^2)$ can be calculated in terms of the twist expansion,

$$\Gamma(Q^2) = \sum_{\tau=2,4...} \frac{\mu_\tau(Q^2)}{(Q^2)^{\frac{\tau-2}{2}}}, \tag{5.11}$$

where $\mu_\tau(Q^2)$ are matrix elements of quark-gluon operators which scale like $\Lambda^{\tau-2}_{\rm QCD}$. The Q^2-dependence in μ_τ are logarithmic and can be calculated in perturbative QCD. If the nucleon mass were zero, $\mu_\tau(Q^2)$ would contain only twist-τ operators. The effect of the nucleon mass is to induce contributions to $\mu_\tau(Q^2)$ from lower twist operators, as we shall illustrate below.

The leading term in Eq. (5.11) is well-known,

$$\mu_2 = \frac{1}{2} \sum_{f=u,d,s...} e_f^2 a_{0f}, \tag{5.12}$$

where the summation covers quarks of all flavors f and a_{0f} is the axial charge defined by the matrix element of axial current $A^\mu_f = \bar{\psi}_f \gamma^\mu \gamma_5 \psi_f$: $\langle PS|A^\mu_f|PS\rangle = 2a_{0f}S^\mu$. The QCD radiative corrections have been calculated to the first order in $\alpha_s(Q^2)$ [46] for the singlet contribution ($a_0^S = 2(a_{0u}+a_{0d}+a_{0s})/9$) and to the third order [47] for the non-singlet contribution ($a_0^{NS} = (2a_{0u} - a_{0d} - a_{0s})/9$). The proton-neutron difference of the moment defines the Bjorken sum rule,

$$\mu_2^p(Q^2) - \mu_2^n(Q^2) = \frac{g_A}{6}\left[1 - \frac{\alpha_s(Q^2)}{\pi} - 3.58\left(\frac{\alpha_s(Q^2)}{\pi}\right)^2 - 20.2\left(\frac{\alpha_s(Q^2)}{\pi}\right)^3 + ...\right], \tag{5.13}$$

where $g_A = a_{0u} - a_{0d} = 1.257$ is the neutron decay constant.

The $1/Q^2$ power corrections to Γ were first studied by Shuryak and Vainshtein (SV) [59]. Using the collinear expansion technique [49], Ji has calculated in Ref. [50] the entire $1/Q^2$ corrections to the g_1 scaling function in terms of a few multi-parton distribution functions. Specializing to the first moment, we find

$$\begin{aligned} \mu_4 &= \frac{1}{9}\sum_f e_f^2\Big[a_{2f} + d_{2f} - 4f_{2f}\Big]M^2 \\ &= (A + D + F)M^2. \end{aligned} \tag{5.14}$$

where $A = \frac{1}{9}\sum_f e_f^2 a_{2f}$ comes from the twist-two contribution and a_{2f} is defined as,

$$\langle PS|\bar{\psi}_f \gamma^{(\sigma}\gamma_5 iD^{\mu_1} iD^{\mu_2)}\psi_f|PS\rangle = 2a_{2f} S^{(\sigma}P^{\mu_1}P^{\mu_2)}, \tag{5.15}$$

with $(\cdots)$ denotes symmetrizing the indices and subtracting the trace; $D = \frac{1}{9}\sum_f e_f^2 d_{2f}$ comes from the twist-three contribution and d_{2f} is defined as,

$$\langle PS|g\bar{\psi}\tilde{F}^{\sigma(\mu_1}\gamma^{\mu_2)}\psi|PS\rangle = 2d_{2f} S^{[\sigma}P^{(\mu_1]}P^{\mu_2)}, \tag{5.16}$$

with $[\cdots]$ denotes anti-symmetrizing the indices and $\tilde{F}^{\sigma\mu_1} = 1/2\epsilon^{\sigma\mu_1\alpha\beta}F_{\alpha\beta}$ is the dual of the gluon field tensor; $F = -\frac{4}{9}\sum_f e_f^2 f_{2f}$ comes from the twist-four contribution and f_{2f} is defined as,

$$\langle PS|g\bar{\psi}_f\tilde{F}^{\mu\nu}\gamma_\nu\psi_f|PS\rangle = 2f_{2f}M^2S^\mu. \tag{5.17}$$

We note that the result quoted for μ_4 in Ref. [59] is $(2A + 2D + F)M^2$.

To study the QCD radiative corrections to μ_4, one has to consider operator-mixing from gluon operators, the anomalous dimensions of which are not currently available and their matrix elements are difficult to estimate. Therefore, in the following discussion, we neglect entirely the scale dependence of μ_4.

The higher twist operators in Eqs. (5.16) and (5.17) depend explicitly on gauge fields. To calculate their matrix elements we need a wave function of the nucleon containing gluon components. However, for special types of higher twist operators such as the present case, we can eliminate the gluons in terms of the "bad" components of quark fields using the QCD equations of motion [50]. Then the higher twist matrix elements can be related to moments of parton distributions with no explicit gluon fields. Indeed, by defining in the light-cone gauge $(A \cdot n = 0)$,

$$g_{(1,T,3)f}(x) = \frac{1}{2}\int \frac{d\lambda}{2\pi} e^{i\lambda x}\langle PS|\bar{\psi}_f \not{Q}_{(1.T,3)}\gamma_5\psi_f(\lambda n)|PS\rangle, \tag{5.18}$$

where $Q_1 = n, Q_T = -S_T/M, Q_3 = -2p/M^2$ and n and p are two null vectors

($n^2 = p^2 = 0$ and $p \cdot n = 1$), we find,

$$
\begin{aligned}
d_{2f} &= \frac{1}{2}\int x^2(3g_{2f}(x) + 2g_{1f}(x))dx, \\
f_{2f} &= \frac{1}{2}\int x^2(7g_{1f}(x) + 12g_{2f}(x) - 9g_{3f}(x))dx,
\end{aligned} \tag{5.19}
$$

where $g_{2f} = g_{Tf} - g_{1f}$. These relations are exact in QCD.

We choose to estimate the $1/Q^2$ corrections to the sum rule in the simplest version of the MIT bag model, in which the bag boundary simulates gluon confinement [51, 52]. Using $g_{if}(x)$ ($i = 1, T, 3$) calculated in this model, we obtain for the proton, $A^p = 0.0065$, $D^p = 0.0092$, and $F^p = 0.0155$. Inserting them into Eq. (5.14), we have,

$$\mu_4^p(\text{Bag}) = 0.031M^2. \tag{5.20}$$

Compared with the size of $\mu_2^p = 0.126 \pm 0.025$ from the EMC data or 0.175 from the Ellis-Jaffe sum rule, the bag $1/Q^2$ power correction is about 10% at $Q^2 = 2$ GeV^2 and about 2% at $Q^2 = 10$ GeV^2. Assuming there are no abnormal twist-six or higher contributions, we conclude that most Q^2 variations of the proton sum rule occur below 1 GeV^2. For the neutron, the bag model predicts, $A^n = D^n = F^n = 0$, and the $1/Q^2$ correction vanishes:

$$\mu_4^n(\text{Bag}) = 0. \tag{5.21}$$

This follows from the SU(6) structure of the bag wave function, which also predicts $\mu_2^n = 0$.

The higher twist matrix elements have also been calculated using the QCD sum rule (QSR) technique by Balitsky *et al* [53]. Their most recent result in terms of our notation is

$$
\begin{aligned}
\mu_4^p(\text{QSR}) &= -(0.023 \pm 0.015)M^2, \\
\mu_4^n(\text{QSR}) &= -(0.006 \pm 0.004)M^2.
\end{aligned} \tag{5.22}
$$

Thus, the QCD sum rule calculation gives a power correction the same size as the bag calculation with the correction for the neutron being significantly smaller than for the proton. However, the sign of the correction differs from the bag result in Eq. (5.20). This difference has a large effect on the Bjorken sum rule at small Q^2.

The Bjorken sum rule has recently been extracted from the data on the proton [38] and neutron [39] g_1 structure functions,

$$\begin{aligned} \int_0^1 g_1^{p-n}(x, 2\ \mathrm{GeV}^2)dx &= 0.146 \pm 0.021[39], \\ &= 0.152 \pm 0.025[54]. \end{aligned} \tag{5.23}$$

In QCD, the Bjorken sum rule at low Q^2 is contaminated by higher twist corrections discussed above. If the QSR result is used for the correction, one obtains a theoretical prediction at the same Q^2,

$$\int_0^1 g_1^{p-n}(x, 2\ \mathrm{GeV}^2)dx = 0.160[54], \tag{5.24}$$

On the other hand, the bag result produces,

$$\int_0^1 g_1^{p-n}(x, 2\ \mathrm{GeV}^2)dx = 0.182. \tag{5.25}$$

While Eq. (5.24) gives a corrected Bjorken sum rule within the experiment errors, the bag calculation disagrees with the extraction of the sum rule by the E142 collaboration by 1.7σ and with the extraction by Ellis-Karliner by 1.2σ. In our opinion, a deviation from the Bjorken sum rule means either a measurement of higher twist matrix elements, or that the data are inconsistent.

From the high and low Q^2 knowledge of the sum rule, we propose a model for $\Gamma^p(Q^2)$ in the entire Q^2 region,

$$\Gamma^p(Q^2) = \frac{1}{2}F_1(F_1 + F_2)(1 - \lambda_1\frac{Q^2}{M^2}) + \lambda_2\frac{1 + \lambda_3 M^2/Q^2}{1 + \lambda_4 M^4/Q^4}, \tag{5.26}$$

where the first term is the elastic contribution with its derivative modified by the

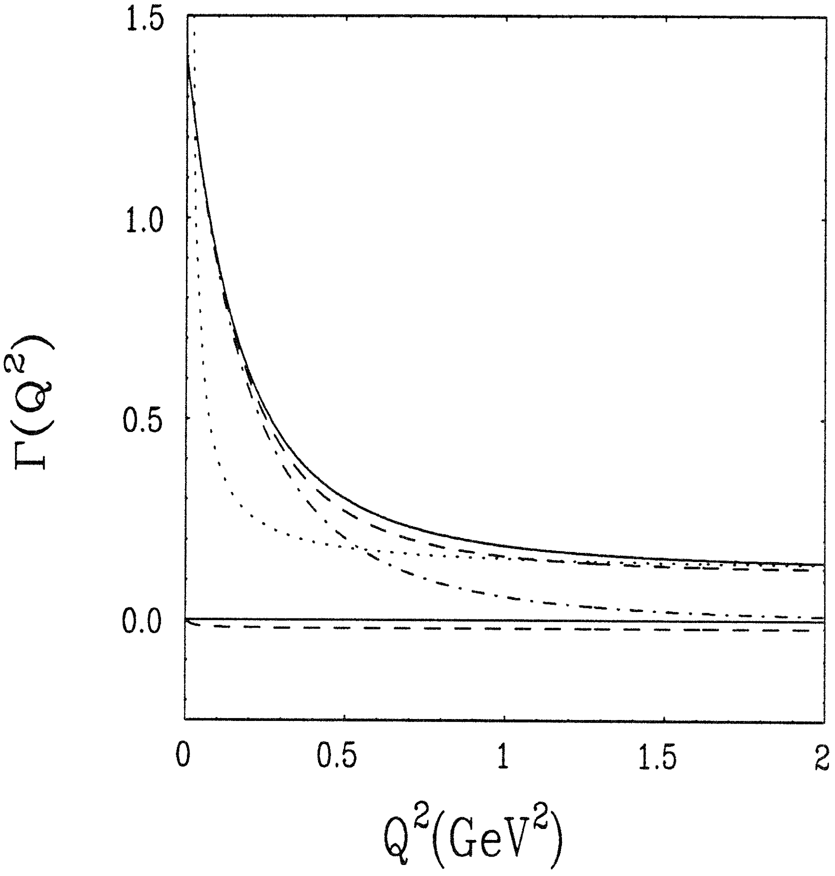

Figure 5-1: A model for the sum rule $\Gamma(Q^2)$ at all Q^2. The meaning of the curves is explained in the text.

Q^2 term. The second term is basically $a + b/Q^2$ and the denominator serves to suppress the contribution at small Q^2. From the EMC data and the various constraints derived above, we determine all λ_i except λ_4, which controls the size of the twist-six contribution. The solid and upper-dashed curves shown in Fig. 5-1 are our parameterization with the bag and QSR higher twist matrix elements, respectively. [We choose $\lambda_4 = 0.3$, which gives a $\mu_6 \sim -0.03$.] The dotted curve represents the result of the twist expansion to order $1/Q^2$ and the dot-dashed curve represents the elastic contribution. As can be seen from the figure, the different choices for higher twist matrix elements result in about 15% difference in Γ in the $Q^2 = 0.5$ to 1.0 GeV^2 region. A similar interpolation is made for the neutron, and the result is shown as the lower-dashed curve.

Thus it appears that the Q^2 variation of the $\Gamma(Q^2)$ sum rule is quite simple. Nevertheless, its experimental measurement is interesting, particularly around $Q^2 =$ 0.5 GeV^2. If we know $\Gamma(Q^2)$ in an extended Q^2 region, we can fit data with a parameterization similar to the one used in Eq. (5.26). Then by expanding in a $1/Q^2$ power series, we can extract the higher-twist matrix elements, such as f_{2f}, which shall provide valuable insight into the spin structure of the nucleon.

Chapter 6

Resonances and Higher Twists, Duality

In electron-nucleon scattering, one probes the substructure of the nucleon with virtual photons of mass Q^2 and energy ν. Before the advent of Quantum Chromodynamics (QCD), Bloom and Gilman [55] discovered an interesting phenomenon about the nucleon structure function $W_2(\nu, Q^2)$, measured at SLAC. Simply speaking, when expressed in terms of the improved scaling variable $\omega' = 1 + W^2/Q^2$, where W is the final-state hadron mass, the scaling function $F_2(Q^2, \omega') = \nu W_2/m_N$ in the resonance region ($W < 2$ GeV) roughly averages to (or duals) that in the deep-inelastic region ($W > 2$ GeV). Referring to a similar phenomenon observed in hadron-hadron scattering, they called it *parton-hadron duality.* Moreover, the occurrence of the duality appears to be local, in the sense that it exists for each interval of ω' corresponding to the prominent nucleon resonances. In fact, the assumption of an exact local duality allows an approximate extraction of the nucleon's elastic form factor from the deep-inelastic scaling function!

An explanation of the Bloom-Gilman duality in QCD was offered by de Rujula, Georgi, and Politzer in 1977 [56]. Following the operator product expansion, they studied the moments of the scaling function in the Nachtmann scaling variable $\xi = 2x/(1+\sqrt{1+4x^2m_N^2/Q^2})$, where $x = Q^2/2m_N\nu$. They argued that the n-th moment

$M_n(Q^2)$ of F_2 has the following twist expansion,

$$M_n(Q^2) = \sum_{k=1}^{\infty} \left(\frac{nM_0^2}{Q^2}\right)^{k-1} B_{n,k}(Q^2)\,, \tag{6.1}$$

where M_0^2 is a mass scale $\sim (400 \sim 500\mathrm{MeV})^2$ and $B_{n,k}(Q^2)$ depends logarithmically on Q^2 and is roughly on the order of $B_{n,0}$. According to Eq. (6.1), there exists a region of n and Q^2 ($n \le Q^2/M_0^2$), where the higher twist contribution is neither large nor negligible, and where the dominant contribution to the moments comes from the low-lying resonances. The appearance of local duality reflects the very existence of this region. A more recent study on duality can be found in Ref. [57].

While these original studies of the parton-hadron duality were largely qualitative, enormous progress has been made in understanding QCD in the past twenty years. The radiative corrections have been evaluated to the next-to-leading order for the twist-two part of the scaling function [58]; the structure of the higher twist expansion has been clarified to the order of $1/Q^2$ and some at the order of $1/Q^4$[59]. The physics of the parton-hadron duality has been exploited ingeniously in the vacuum correlation functions, from which a powerful technique for calculating hadron properties from QCD—the QCD sum rule method—has emerged [60]. Experimentally, a large body of lepton-nucleon scattering data has been collected in the past 25 years [61]. With the CEBAF facility becoming available for making systematic, high precision measurements in the resonance region, it is timely to re-examine duality in its original context, and further explore the physics content of this important concept.

In this chapter we seek to sharpen the explanation of the duality offered by authors in Ref. [56], with a few crucial differences. First, we choose to work with the moments of Cornwell-Norton, instead of those of Nachtmann, thereby avoiding the unphysical region of $\xi > \xi(x=1)$. Second, we look for a way to describe more clearly the contribution of the resonances to the moments. Finally, we emphasize a thorough exploitation of the consequences of duality. We furnish our discussions with the example of F_2, for which the abundant data allow an accurate construction of its moments in the low and medium Q^2 region. These moments offer a unique opportunity for studying the effects of higher twists and the resonance contributions.

6.1 Parton-Hadron Duality Revisited

The Cornwell-Norton moments of a scaling function $F(x, Q^2)$ are defined as,

$$M_n(Q^2) = \int_0^1 dx x^{n-2} F(x, Q^2) , \tag{6.2}$$

where the upper limit includes the elastic contribution. According to the operator production expansion, the moments can be expanded in powers of $1/Q^2$,

$$M_n(Q^2) = \sum_{k=0}^{\infty} E_{nk}(Q^2/\mu^2) M_{nk}(\mu^2) \left(\frac{1}{Q^2}\right)^k , \tag{6.3}$$

where E_{nk} are the dimensionless coefficient functions which can be calculated perturbatively as a power series in the strong coupling constant $\alpha_s(Q^2)$,

$$E_{nk}(Q^2/\mu^2) = \sum_{i=0}^{\infty} \alpha_s^i(Q^2) e_{nk}^i , \tag{6.4}$$

and $M_{nk}(\mu^2)$ are the nucleon matrix elements of local operators composed of quark and gluon fields. The renormalization scale (μ^2) dependence cancels in the product of the two quantities; however, when we talk about them separately, μ^2 is chosen to be the hadron mass scale. The terms beyond the first in Eq. (6.3) are called the higher-twist corrections, which include both the target mass corrections and the true higher-twist effects.

The double expansions in Eq. (6.3) are asymptotic at best. Non-perturbative effects can invalidate both expansions at higher orders, and can mix the two, rendering the separation of radiative and power corrections ambiguous [62]. In the following discussion, however, we assume that in the Q^2 region of our interest, the size of the twist-four term ($1/Q^2$) is significantly larger than the smallest term in the asymptotic expansion for E_{n0}, beyond which the evaluation of E_{n0} cannot be improved by including higher-order terms, and so the ambiguity in defining the higher-twist corrections

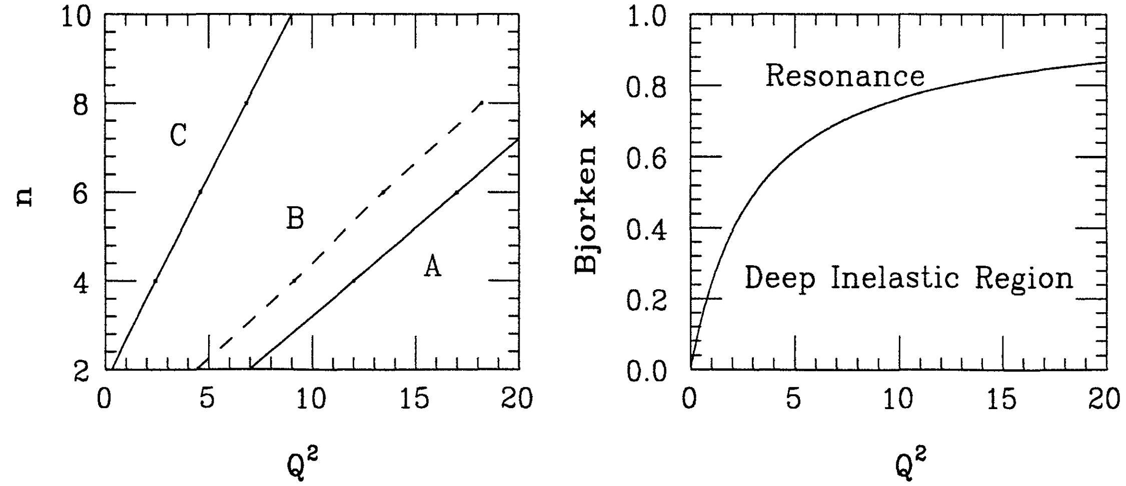

Figure 6-1: a). Three regions of differing importance to higher twists: Region A, negligible higher twists; Region B, perturbative higher twists; and region C, the twist-expansion breaks down. b). Kinematic regions corresponding to the resonance and deep-inelastic scattering.

can be neglected [62]. We shall henceforth focus only on the structure of the twist expansion.

Following Ref. [56], we assume the ratio of the twist-four term to the leading twist in each moment is approximately nM_0^2, where M_0 is a scale characterizing the matrix elements of the twist-four operators. We further assume that the twist expansion is an asymptotic series in the parameter nM_0^2/Q^2. According to the above assumptions, we can classify the higher-twist contributions to the moments. Consider the $n - Q^2$ plane as shown in Fig. 6-1(a), which is separated into three regions by two solid lines. Region A is defined by $nM_0^2 \ll Q^2$, where the higher-twist effect are negligible. Region B is where the higher-twist corrections become important but stay perturbative, and thus only the first few terms in the twist-expansion are of practical importance. Region C is where the higher-twist effects become non-perturbative, and the power-expansion loses meaning. It is in this third region that the resonance physics dominates the behavior of the moments and the quantum coherence, inherent to resonance production, defies a description of the scattering in terms of a finite number of quarks and gluons. In the later part of the chapter, we will show that the first assumption is consistent with the behavior of the lower moments for F_2.

Now we consider the resonance contribution to the Cornwell-Norton moments by examining the $x - Q^2$ plane shown in Fig. 6-1(b), in which the resonance region is approximately above the curve $W = 2$ GeV. For a large, fixed Q^2 (say 15 GeV^2), the resonance contribution to the lowest few moments is very small, and can be neglected. When n increases, the resonance contribution is weighted more and becomes significant. We can use a dashed line, as Q^2 varies, in the $n - Q^2$ plane to indicate the separation of the two cases. The dashed line certainly cannot be in region A, because the non-resonance experimental data have already detected the higher-twist effects [65]. If the dashed line is in the region C, then the perturbative higher-twist effects have nothing to do with resonance physics. The most exciting possibility is when the dashed line lies in the region B, and this is what happened in reality.

When the dashed line is located in region B, then in the left portion of it, the following statements are true: 1). the higher-twist corrections are perturbative, so the moments are not too different from those at larger Q^2, and 2). the resonance contribution to the moments are significant. Thus in this region, the resonances must organize themselves to follow the deep-inelastic contribution apart from a perturbative higher-twist correction, or conversely, the structure of the higher-twist expansion constrains the behavior of the resonance contribution. The degree of duality is determined by the size of this region: the larger the region, the more the moments are constrained, and the more local the duality will be.

Why should duality occur at all in QCD? On one hand, the quark transverse momentum in the nucleon, which governs the magnitude of the higher-twists, is about

400 MeV. This makes the higher-twist corrections perturbative down to very small Q^2. On the other hand, the resonance contribution to the moments are already significant at $Q^2 \sim 5\text{GeV}^2$ for low n. Thus the occurrence of the duality seems unavoidable, unless QCD had two widely different scales.

The consequences of duality, like duality itself, are two-fold. If one knows data in the resonance region, one can extract the matrix elements of the higher-twist operators. The extraction, of course, is limited by our ability to calculate higher-order radiative corrections, about which we have nothing to say. On the other hand, if one knows the higher-twist matrix elements from other sources, such as lattice QCD calculations, one can utilize them to extract the properties of the resonances. This second use of duality has been pursued extensively in the QCD sum rule calculations, from which a large number of interesting results has been obtained [60]. In the present case, however, the number of higher-twist matrix elements is large, and they are difficult to estimate in general. This severely limits our ability to check, for example, the internal consistency of the duality predictions.

6.2 Twist-Four Matrix Elements from $F_2(x, Q^2)$

We make the above discussion more concrete and quantitative by using the example of the F_2 scaling function, for which rich data exist in an extended kinematic region. Most of the low Q^2 data were taken in late 60's and early 70's at SLAC and DESY, and they nearly cover the whole resonance region at large x. The data were fitted by Brasse *et al.* [63] to a function with three parameters for each fixed W. In Ref. [64], Bodek *et al.* have made a more extensive but different fit, covering higher Q^2 resonance data. The deep-inelastic data were systematically taken by SLAC, BCDMS, EMC, and other collaborations during the 70's and 80's, and they have recently been shown to be consistent with each other [65]. New measurements from NMC at CERN has extended these data to lower Q^2 and x [66]. In Fig. 6-2. we have shown the F_2 data as a function of Bjorken x at $Q^2 = 0.5, 1.0, 2.0, 4.0, 8.0$ and 16.0 GeV^2 from the two fits [64, 66] made in different kinematic regions.

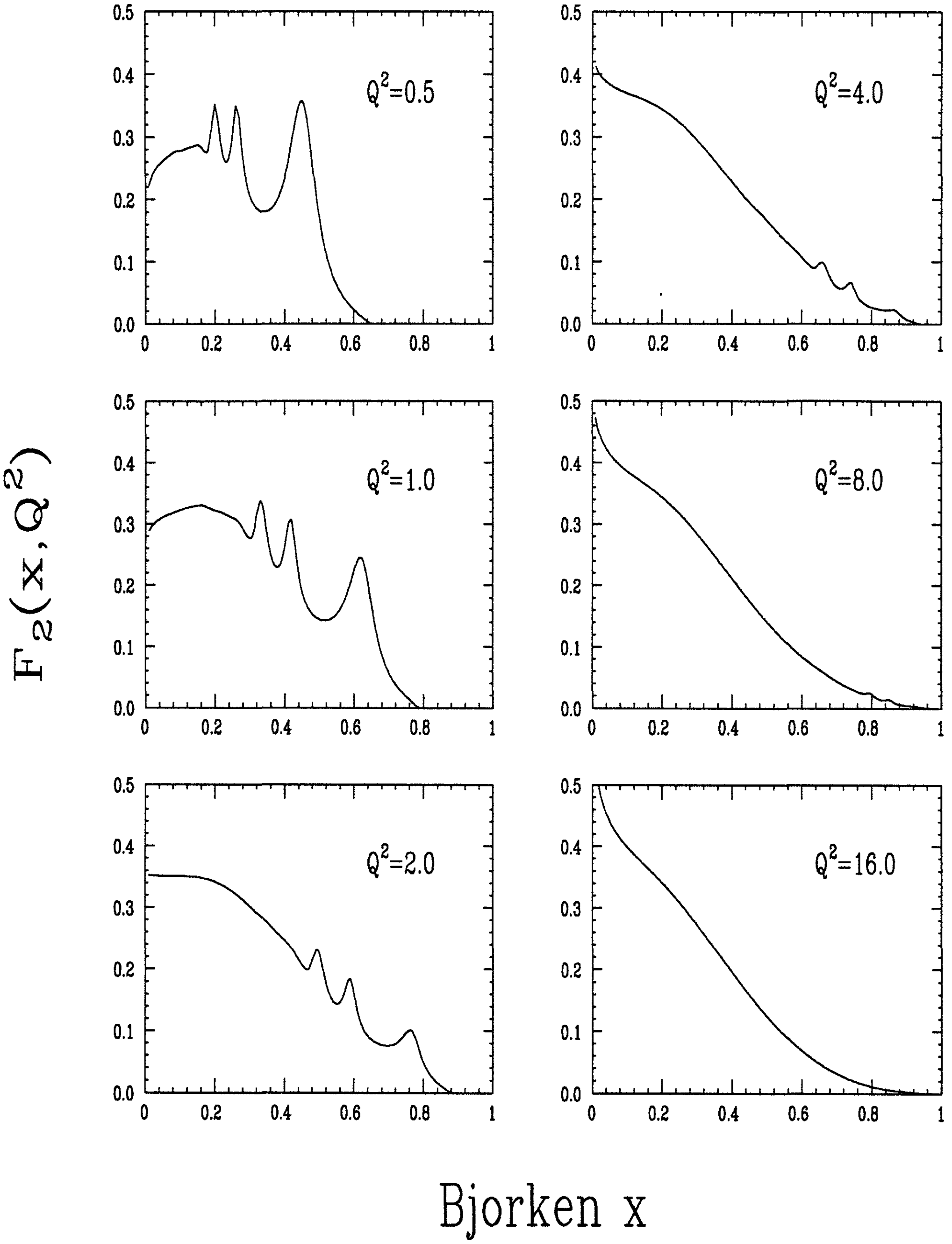

Figure 6-2: Scaling function obtained from the fits to experimental data in Refs. [64, 66].

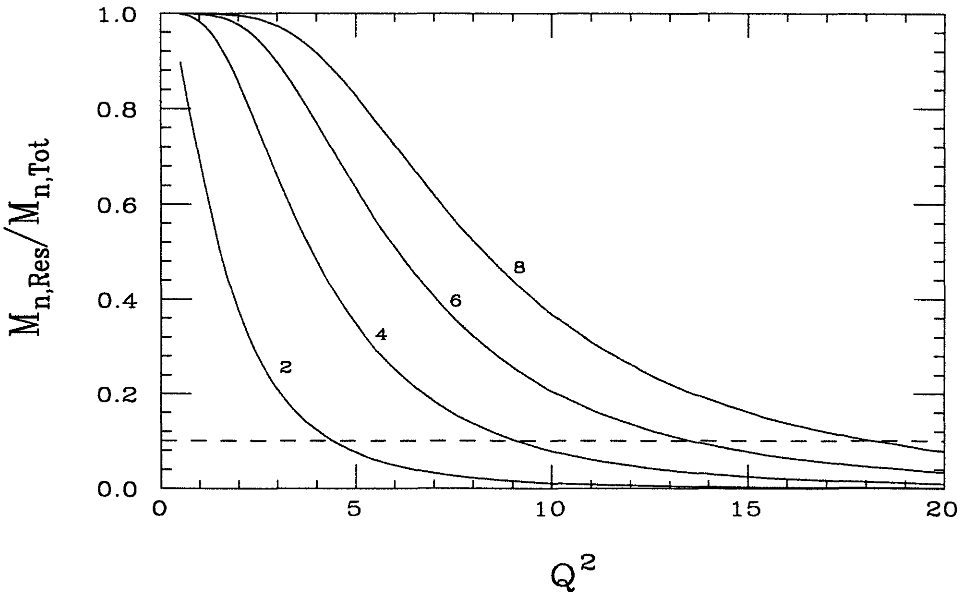

Figure 6-3: Ratio of the moments from the resonance region, including the elastic contribution, to that of the total.

The salient features of the data can be summarized as follows. At high-Q^2, the data is almost entirely deep-inelastic except for a small resonance contribution at large x. The scaling function near $x = 0$ shows a rise due to perturbative QCD effects. As Q^2 decreases, small bumps become visible and slide toward low x. These prominent excitations are believed to be the $\Delta(1232)$, $S_{11}(1535)$ or $D_{13}(1520)$, and $F_{15}(1680)$ resonances. The resonance excitations become very strong near $Q^2 = 2$ GeV^2 and clearly dominates F_2 below $Q^2 = 1$ GeV^2. As $Q^2 \to 0$ the data is compressed toward $x = 0$ due to simple kinematics. At $Q^2 = 0$, the whole photo-production physics is shrunk to $x = 0$. Of course, one should not forget about the elastic contribution, which contributes a delta-function at $x = 1$.

To understand the role of the resonances in the Cornwell-Norton moments, we plot in Fig. 6-3. the ratio of the resonance part to the total, where the resonance contribution is defined by a cut on $W < 2$ GeV. If one uses ten percent as a measure of the importance of the resonance contribution, then this threshold is reached for the lowest moment($n = 2$) at $Q^2 \sim 4$GeV^2. For higher moments, the transition occurs

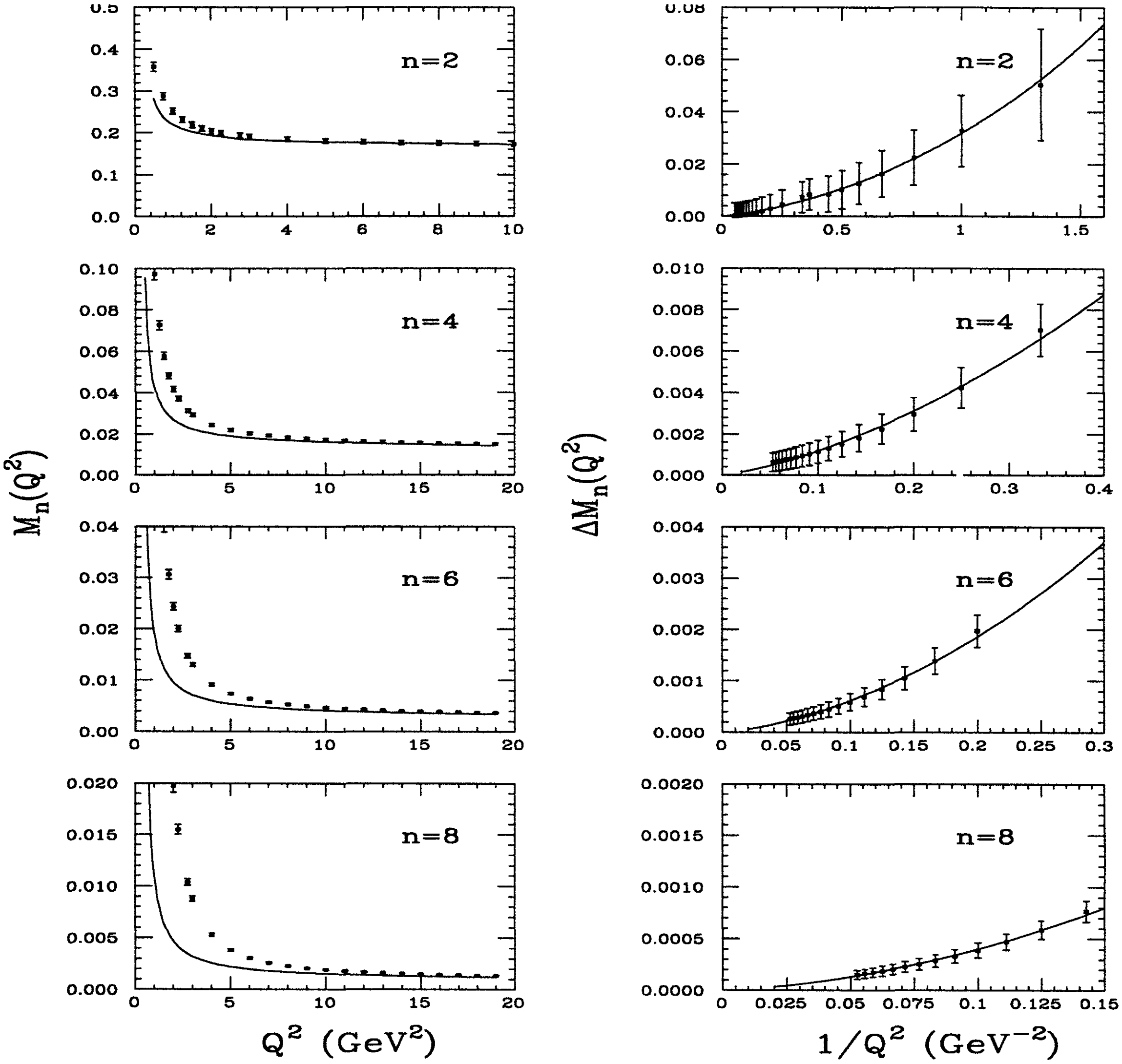

Figure 6-4: a). Moments as functions of Q^2, extracted from the scaling function in Fig. 6-2. The solid lines refer to the contribution from the leading twist and target-mass corrections. b). Residue moments from the higher-twist contribution. The solid lines are the fits described in the text.

approximately at $2n$ GeV^2. This is quite surprising because the non-perturbative physics becomes potentially important at $Q^2 = 16$ GeV^2 for the 8th moment! At $Q^2 = 8$ GeV^2, the same moment receives fifty percent of the contribution from the resonance region. The dashed line in Fig. 6-1(a) roughly corresponds to the ten percent line shown in Fig. 6-3. The data on the F_2 moments can be used to extract the matrix elements of higher-twist operators. To effect this, we first subtract the twist-two part of the contribution. We use a parton distribution (CTEQ2, [67]) fitted to a large number of data on hard processes, and calculate the moments for each quark flavor and gluon distribution at some large Q^2 (=20 GeV^2 in our case). Then we evolve these moments to lower Q^2 using the perturbative QCD formula accurate to next-to-leading order. Theoretical errors in evolution are mainly generated from uncertainty in $\Lambda_{\rm QCD}$ and unknown higher-order terms in the coefficient functions. In our work, we take $\Lambda^{(4)}_{\rm QCD} = 260 \pm 50$ GeV [68], and the resulting error is added to the experimental error which is taken to be 3% uniformly, yielding the total error on the residue. The target mass corrections are further subtracted from the moments according to the formula in Ref. [69]. In Fig. 6-4(a), we show the moments as a function of Q^2 and the twist-two part plus the target mass corrections (solid lines). The residual moments, which are entirely higher twist effects, are shown in Fig. 6-4(b) as functions of $1/Q^2$.

We choose to fit the Q^2 evolution of the moments with a pure twist-four contribution,

$$\Delta M_n(Q^2) = a_n \left(\frac{\alpha(Q^2)}{\alpha(1)}\right)^{\gamma_n} \frac{1}{Q^2} \tag{6.5}$$

where we have included phenomenologically the leading-log effects with an adjustable exponent. The fitted γ_n represents an average of the anomalous dimensions of the spin-n, twist-four operators, weighted by the size of individual matrix element. The coefficient a_n is a simple sum of the twist-four matrix elements at the scale $\mu^2 = 1$ GeV^2. Inclusion of a twist-six term creates strong correlations among the parameters and renders the fits indeterminate. Thus we have neglected such a term by restricting the fit to the region with $Q^2 > n$, where the twist-six contribution is presumably small.

n	$a_n(\text{GeV}^2)$	γ_n	$a_n/(E_{n0}M_{n0})$	M_0
2	0.030 ± 0.003	1.0 ± 0.5	0.14	0.26
4	0.042 ± 0.013	1.5 ± 0.5	1.00	0.50
6	0.047 ± 0.021	2.5 ± 0.5	2.47	0.64
8	0.038 ± 0.018	2.5 ± 0.5	3.45	0.66
10	0.052 ± 0.025	3.5 ± 0.5	4.73	0.69

Table 6.1: Extracted twist-four coefficients a_n, leading log parameters γ_n, followed by an extracted mass scale in the final column.

The result of our fit is shown in Table 6.1. The correction to the $n = 2$ moment (the famous momentum sum rule) is best determined, yielding a characteristic higher-twist scale of 500 MeV. From this, we determine that the twist-four contribution to the momentum sum rule at $Q^2 = 2$ GeV^2 is 0.015, about ten percent of the total. The exponent of the leading-log contribution increases gradually with n, in accord with general expectations. The near constancy of the twist-four contribution is in sharp contrast with the fast decrease of the leading-twist contribution with increasing n. It confirms, though, the speculation that the higher-twist contribution become more important for higher moments, and is a precursor for the onset of the resonance region. In QCD, this can be explained by an increasing number of twist-four operators compensated by a decrease in strength of individual matrix elements. The pattern of the moments indicates a twist-four distribution negative at small x, positive at large x and peaked near $x = 1$, qualitatively consistent with the fits in Ref. [65], where the resonance data were entirely ignored.

Finally, we test the assumption about the higher-twist matrix elements in Eq. (6.1). We show in the fourth column of Table 6.1 the ratio of the higher-twist matrix elements and the twist-two part. From this, we extract an effective M_0 by dividing by n and taking the square root. The result is shown in the fifth column and is approximately n-independent, although there is a slight hint of M_0 getting larger for larger n. However, this should not be taken too seriously because of the errors and limited number of moments. If fifty percent of the higher-twist contribution is taken as an indication that the twist-expansion is getting non-perturbative, we find a Q^2

for each moment where the transition takes place. For $n = 2$, this is about 0.3 GeV^2. For higher moments, this happens at about $n - 1$ GeV^2. The line which separates regions B and C in Fig. 6-1 roughly corresponds to this. Thus the existence of the duality zone is clearly established beyond any doubt.

To illustrate the other use of duality, one could, for instance, use the higher-twist contribution extracted from the pure deep-inelastic region (as done in [65]), or from some theoretical calculations, to determine the nucleon's elastic form factor. However, we feel that the higher-twist matrix elements have not been determined in other methods to a sufficient accuracy to allow a quantitative extraction of the resonance properties. Qualitatively, however, knowing the higher-twist contribution will surely improve the nucleon form factor extracted in Ref. [56], which shows a systematic deviation from the directly measured G_M, a clear indication of higher-twist effects.

To sum up, we explored in this work the physics of the parton-hadron duality. We emphasized that the existence of duality allows one to determine the higher twist matrix elements from data in the resonance region, or alternatively, knowing the matrix elements enables one to determine the properties of the resonances. We studied the duality picture offered by the F_2 scaling function, and extracted the matrix elements of the lowest few spin, twist-four operators. Clearly, this study can be applied straightforwardly to the spin-dependent structure function G_1 once more data becomes available.

Appendix A

Bag Model Calculations

The MIT bag model is an attempt to simulate nonperturbative aspects of QCD. Confinement is provided explicitly by confining the quark and gluon fields within the bag. We quickly review the bag model and extract the following three distributions: $g_1(x)$, $g_2(x)$ and $g_3(x)$. Our discussion will be limited to the cavity approximation where there are no gluon fields and quantum fluctuations are ignored. The equations of motion satisfied by the quark fields are then simply,

$$\begin{aligned} -i\partial\!\!\!/ q_\alpha(x) &= 0 \quad (x \text{ in bag}) && \text{(A.1)} \\ i n\!\!\!/ q_\alpha(x) &= q_\alpha(x) \quad (x \text{ on bag surface}) && \text{(A.2)} \\ n^\mu \partial_\mu \sum_\alpha \bar{q}(x)_\alpha q(x)_\alpha &= 2B \quad (x \text{ on bag surface}) && \text{(A.3)} \end{aligned}$$

Where n is the inward pointing four vector normal to the bag boundary and B is the bag pressure. The bag boundary conditions allow quark helicity flips, even though the quarks are massless. This can seen from the second boundary condition as the normal vector does not commute with the helicity projectors $(1 \pm \gamma_5)/2$. Thus the model has nontrivial spin dependent dynamics.

The solutions within the cavity factor into radial and angular solutions. Applying the boundary condition (A.2) specifies the eigenfrequency of the n'th radial mode,

$$\tan(\omega_n) = \frac{\omega_n}{1 - \omega_n} \tag{A.4}$$

The lowest energy mode being given by $\omega_0 = 2.04278...$ Further it can also be shown [70] that the proton mass and bag radius are related thru $RM = 4\omega_0$. This is accomplished by replacing Eq. (A.3) with an energy variational principle where the bag pressure stabilizes the system. Fourier transforming the lowest mode yields the momentum space representation of the cavity wavefunctions [71].

$$\phi(\vec{p}) = i\left(\frac{2}{\pi}\right)^{1/2} \frac{R_0^3}{\sqrt{N(\omega)}} \begin{pmatrix} t_0(\omega, pR_0)\ U_m \\ t_1(\omega, pR_0)\ \vec{\sigma}\cdot\vec{p}\ U_m \end{pmatrix} \tag{A.5}$$

Where, U_m is a Pauli spinor and,

$$t_l(\alpha,\beta) = \int_0^1 dx x^2 j_l(\alpha x) j_l(\beta x) \tag{A.6}$$

$$N(\omega) = 4\pi R_0^3\big(t_0(w,w) + t_1(w,w)\big) \tag{A.7}$$

The ingredients now being present we apply the bag model to calculating the g_i distributions, used in Chapter Five. The distributions $g_1(x)$ and $g_2(x)$ have been calculated previously by Hughes [71] and again correctly by Jaffe and Ji [72]. Applying the cavity approximation results in,

$$g_1(x) = \Omega \int_{|y_m|}^{\infty} dyy\left(t_0^2 + 2t_0t_1\frac{y_m}{y} + t_1^2\left(\frac{2y_m^2}{y^2} - 1\right)\right) + \{x \to -x\} \tag{A.8}$$

$$g_2(x) = \Omega \int_{|y_m|}^{\infty} dyy\left(-2t_0t_1\frac{y_m}{y} + t_1^2\left(\frac{-3y_m^2}{y^2} + 1\right)\right) + \{x \to -x\} \tag{A.9}$$

$$g_3(x) = \Omega\frac{M^2}{\Lambda^2} \int_{|y_m|}^{\infty} dyy\left(t_0^2 - 2t_0t_1\frac{y_m}{y} + t_1^2\left(\frac{2y_m^2}{y^2} - 1\right)\right) + \{x \to -x\} \tag{A.10}$$

The normalization factor is given by,

$$\Omega = \frac{5}{18}\frac{4\omega^2}{2\pi j_0^2(\omega)(\omega-1)}, \tag{A.11}$$

and $y_m = (4x-1)\omega$..

The "unfolded" distributions are shown in Fig. A-1. We take the scale factor Λ to be the nucleon mass. Defining the moment $M_n = \int_0^1 g(x)x^n dx$ we calculate the first few in table A.1.

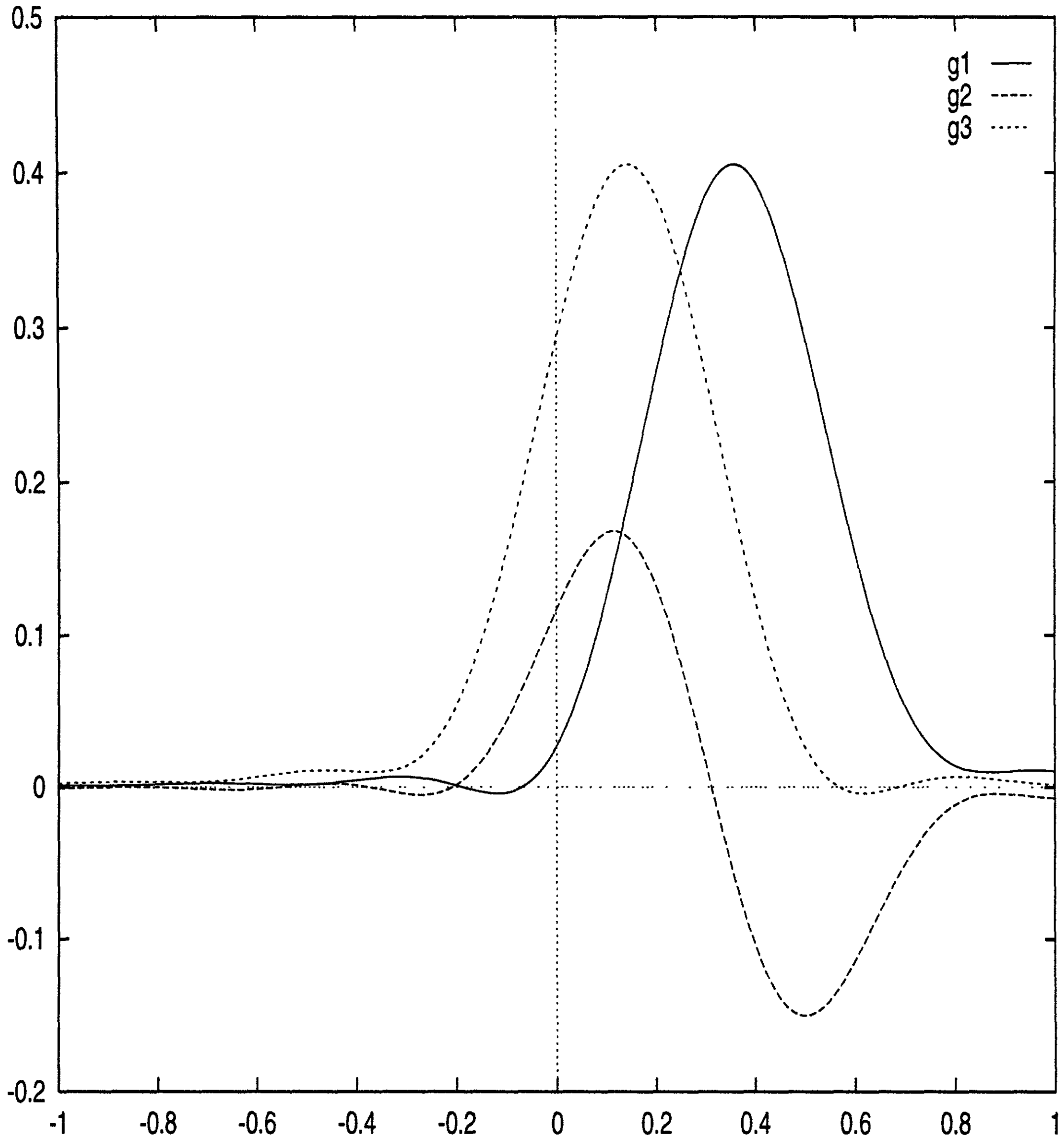

Figure A-1: The three distributions $g_1(x)$, $g_2(x)$ and $g_3(x)$ calculated in the Bag Model. The horizontal axis is Bjorken x.

n	g_1	g_2	g_3
0	0.175	0.000	0.176
2	0.029	-0.013	0.010
4	0.009	-0.005	0.002

Table A.1: The first three even moments of the distributions g_i calculated in the bag model.

Appendix B

Pion Electroproduction and Helicity Amplitudes

Consider the scattering of photons onto hadrons. A significant portion of the total S-matrix amplitude is given by pion production at low energy. We examine the contribution the pion decay channel makes to the inclusive structure functions F_1, F_2, G_1 and G_2, where the final state dependence has been integrated out.

There are a total of twelve complex amplitudes which must be specified to fully characterize pion scattering if no higher symmetries such as parity are considered. Consider first the initial states in the center of mass frame. A photon with momentum q^{μ}_{com} and spatial momentum $\vec{q}$ interacts with a hadron having equal and opposite three momentum. The amplitudes are most easily enumerated in terms of helicity. We specify the photons helicity first, followed by that of the incident spin 1/2 hadron:

$$(1, 1/2), (1, -1/2), (0, 1/2), (0, -1/2), (-1, 1/2), (-1, -1/2) \tag{B.1}$$

The final states will have helicity along $\vec{k}_{com}$ the momentum of the outgoing pion. Since the pion has no spin, and we are assuming the final state hadron is also spin 1/2, we have two possible outgoing helicity states. Therefore a total of twelve complex helicity amplitudes must be specified to characterize the pion decay channel of the reaction.

$$H_{h_f h_i}(|\vec{q}|, \theta, \phi) \tag{B.2}$$

where $h_i = h_{photon} - h_{hadron}$ is the initial helicity and $h_f = -h_{hadron}$ is the final state hadron helicity. where θ is the angle between $\hat{q}$ and $\hat{k}$ and ϕ is zero in the electron scattering plane. These twelve functions of θ and φ the angle of scattering in the x-y plane relative to the x-axis, which for electroproduction we take to be the electron scattering plane, and the helicity indexes, are related by parity so only six are independent. (One further constraint results from an arbitrary phase chosen at will.)

Helicity is a frame dependent quantity because the hadron is massive. One might, therefore prefer to work with states of definite total angular momentum. Experimentalists extract information from the final state by measuring the final state angular coordinates and the spin of the outgoing hadron distributions. Fitting the data with spherical harmonics it is possible to work backwards and find the amplitude of a particular contribution in the J'th channel of total angular momentum. We therefore expand the helicity amplitudes in terms of states of definite parity and angular momentum,

$$H_{h_f,h_i}(\theta, \phi) = \sum_J (2J+1) H^J_{h_f\ h_i} D^J_{h_f\ h_i}(\theta, \phi), \tag{B.3}$$

where $D^J_{h_f\ h_i}$ satisfies,

$$\int d\Omega\ D^{*\,J'}_{h'_f\ h'_i} \cdot D^J_{h_f\ h_i} = \frac{4\pi}{(2J+1)} \delta_{h'_i\ h_i} \delta_{h'_f\ h_f} \delta_{J'\ J}. \tag{B.4}$$

The matrix D^J is the rotation matrix which connects states of constant J. The observed final state is therefore related to a state quantized along the $\hat{q}$ axis with known helicity in the J channel. Resonances tend to contribute in a particular channel, the delta for example contributes mainly with $J = 3/2$, $l = 1$ and is named $\Delta(1232)P_{33}$ to reflect this.

The rotation matrix has the following properties under parity transformations,

$$D^J_{h_f\ h_i}(\theta,\phi) = -e^{i(h_i-h_f)(\pi-2\phi)} D^J_{-h_f\ -h_i}(\theta,\phi) \tag{B.5}$$

(see the appendix C for more properties of the rotation matrix). This condition relates one half of the helicity amplitudes to some reference set by parity. The accepted choice is to take the first four helicity combinations in Eq. (B.1). The amplitudes can be expanded in terms of Jacobi polynomials, themselves expressible as derivatives of more standard Legendre polynomials to give the Walker amplitudes:

$$\begin{aligned}
H_1 e^{i\phi} &= H_{1/2,1+1/2} = \frac{1}{\sqrt{2}} e^{i\phi} \sin(\theta)\cos(\frac{\theta}{2}) \sum_{l=1}^{\infty} (B_{l+} - B_{(l+1)-})(P_l'' - P_{l+1}'') && \text{(B.6)} \\
H_2 &= H_{1/2,1-1/2} = \sqrt{2}\cos(\frac{\theta}{2}) \sum_{l=0}^{\infty} (A_{l+} - A_{(l+1)-})(P_l' - P_{l+1}') && \text{(B.7)} \\
H_3 e^{2i\phi} &= H_{-1/2,1+1/2} = \frac{1}{\sqrt{2}} e^{2i\phi} \sin(\theta)\sin(\frac{\theta}{2}) \sum_{l=1}^{\infty} (B_{l+} + B_{(l+1)-})(P_l'' + P_{l+1}'') && \text{(B.8)} \\
H_4 e^{i\phi} &= H_{-1/2,1-1/2} = \sqrt{2} e^{i\phi} \sin(\frac{\theta}{2}) \sum_{l=0}^{\infty} (A_{l+} + A_{(l+1)-})(P_l' + P_{l+1}') && \text{(B.9)} \\
H_5 &= H_{1/2,0+1/2} = \sqrt{2}\cos(\frac{\theta}{2}) \sum_{l=0}^{\infty} (C_{l+} - C_{(l+1)-})(P_l' - P_{l+1}') && \text{(B.10)} \\
H_6 e^{i\phi} &= H_{-1/2,0+1/2} = \sqrt{2} e^{i\phi} \sin(\frac{\theta}{2}) \sum_{l=0}^{\infty} (C_{l+} + C_{(l+1)-})(P_l' + P_{l+1}'). && \text{(B.11)}
\end{aligned}$$

The notation $l+$ indicates $l = J - 1/2$ and $(l+1)-$ implies $l = J + 1/2$ where l is the pion orbital angular momentum for a given J. The first four amplitudes encompass the transverse polarization of the photon while the last two deal with the longitudinal component.

B.1 Helicity Amplitudes, and Cross Sections

This section discusses the relationship between photoproduction and electroproduction, forward Compton scattering, Walker's helicity amplitudes and experimentally measured cross sections.

The hadronic forward Compton scattering amplitude $\mathrm{T}^{\mu\nu}$ describes the scattering of a photon on a hadron. The word "forward" dictates the scattered virtual photon has equal and opposite momentum to the incident photon. The utility of this restriction is that the cross section for photo or electroproduction is related by the optical theorem to the imaginary part of the forward scattering amplitude. The amplitude is defined by the following tensor:

$$\mathrm{T}^{\mu\nu}_{h',h}(Q^2,\nu) = i\int d^4\xi e^{iq\cdot\xi}\langle p,h'|T\{J^{\mu\dagger}(\xi)J^{\nu}(0)\}|p,h\rangle. \tag{B.12}$$

Where p_μ and h,h' are the nucleon's momentum and initial and final helicity. The electric current of the quarks coupling the hadron to the incident and scattered photon is given by J^ν. The four momentum q_μ transfered by the photon is expressed by the Lorentz invariants $Q^2 = -q^2$ and $\nu = p \cdot q/m_p$. The helicity amplitudes are then defined by saturating the indices of $\mathrm{T}^{\mu\nu}$ with the scattered and incident photon polarizations,

$$T_{h_f,h';h_i,h} = \epsilon^{*f}_{\mu}\ \mathrm{T}^{\mu\nu}_{h',h}\ \epsilon^{i}_{\nu}, \tag{B.13}$$

h_i is the helicity of the incident photon and h_f that of the outgoing photon. When probing this tensor one faces the following restrictions: first, only real photon beams can be prepared experimentally. The incident photon in this case is transversely polarized and has $Q^2 = 0$. The longitudinal components are not sampled and the kinematic range of $\mathrm{T}(Q^2,\nu)$ is restricted to the ν axis. The second experimental possibility is to use electroproduction. The virtual photon has none zero Q^2 and its polarization is determined by the preparation of the electron beam. We will discuss polarization effects in terms of the following polarization basis,

$$\epsilon^{\mu}_{\pm 1} = \mp\frac{1}{\sqrt{2}}(0,1,\pm i,0) \tag{B.14}$$

$$\epsilon^{\mu}_{0} = \frac{\nu}{m_p Q}(\sqrt{1+\frac{m_p^2 Q^2}{\nu^2}},0,0,1) \tag{B.15}$$

where the three momentum of the photon is along the $\hat{z}$ direction, and we work in COM frame.

Having defined the Walker amplitudes previously, we now discuss how they can be recovered from experiment. The differential cross section is described in terms of a contraction between the hadron $\mathrm{W}^{\mu\nu}$ and lepton $\mathrm{L}^{\mu\nu}$ tensors. The hadron tensor is given by,

$$\mathrm{W}^{\mu\nu}_{h',h} = \frac{1}{4\pi}\int d^4\xi e^{iq\cdot\xi}\langle p,h'|J^{\mu\dagger}(\xi)J^{\nu}(0)|p,h\rangle = \frac{1}{2\pi}Im\mathrm{T}^{\mu\nu}_{h',h}. \tag{B.16}$$

Using the following normalization,

$$\langle p',h'|p,h\rangle = 2p^0\cdot(2\pi)^3\cdot\delta^3(\vec{p}-\vec{p}')\sigma_{h',h} \tag{B.17}$$

and inserting a complete set of states into $\mathrm{W}^{\mu\nu}$ and obtain,

$$\mathrm{W}^{\mu\nu} = \frac{(2\pi)^4}{4\pi}\sum_{n=1,h_n}^{\infty}\int\prod_{i=1}^{m}\frac{d^3p_i}{(2\pi)^3\,2p_i^0}\langle p,h'|J^{\mu\dagger}|X_n,h_n\rangle\langle X_n,h_n|J^{\nu}|p,h\rangle\delta^4(p+q-X_n) \tag{B.18}$$

Here the index n runs over the number of particles in the final state and $X_n = \sum_{i=1}^{n}p_i$ is the sum of the final state momenta. One must also sum over the helicities of the final states, represented here by h_n.

We now discuss the contributions from $n=2$ with a pion and hadron in the final state. In the COM, $\vec{q}=-\vec{p}$, leaving only an angular integral over the pion helicity amplitudes,

$$\mathrm{A}_{h_b,h':h_a,h} = \epsilon^{*b}_{\mu}\mathrm{W}^{\mu\nu}_{h',h}\epsilon^{a}_{\nu} = \frac{1}{8(2\pi)^3}\frac{|\vec{p}_1|}{W}\sum_{h_f}\int d\Omega\;\tilde{\mathrm{H}}^{*}_{h_f,h_b-h'}\tilde{\mathrm{H}}_{h_f,h_a-h} \tag{B.19}$$

Here $h_f = h_1 - h_2 = -h_2$ where particle one is the spin zero pion and particle two the spin half hadron. The helicity amplitudes A can now be combined to give expressions for the hadron structure functions. $\tilde{\mathrm{H}}$ is the pion helicity amplitude and the focus of this section.

$$\begin{aligned}\tilde{\mathrm{H}}_{h_1-h_2,h_a-h} &= \langle p_1,h_1;p_2,h_2|\epsilon^{h_a}_{\mu}J^{\mu}|p,h\rangle &\text{(B.20)}\\ &= \langle|\vec{p}_1|,\theta,\phi,-h_2|\epsilon^{h_a}_{\mu}J^{\mu}|p,h\rangle &\text{(B.21)}\end{aligned}$$

(The helicity is specified along the pion momentum.) The amplitudes derived here are directly proportional the Walker's helicity amplitudes discussed previously.

The lepton tensor is normally defined in terms of electron kinematic variables,

$$\mathrm{L}^{\mu\nu} = 2k^\mu k^\nu + (k \cdot q)g^{\mu\nu} - k^\mu q^\nu - k^\nu q^\mu + 2i\epsilon^{\mu\nu\alpha\beta}k_\alpha q_\beta \tag{B.22}$$

Where k is the incident four momentum of the lepton, q is the virtual photon momentum and $\epsilon^{0123} = 1$. We remark here that effects of the $O(m_e^2)$ have been systematically neglected. We would like to rewrite this tensor in terms of photon polarizations, so as to relate the pion helicity amplitudes to standard definitions of the structure functions. Working in the COM frame and choosing the $\hat{z}$ axis along the photon momentum, one can express the antisymmetric parts of the lepton tensor in terms of the photon polarization vectors as follows. The transverse terms are proportional to the following density matrix:

$$\rho_T^{\mu\nu} = \epsilon_+^{*\mu}\epsilon_+^\nu - \epsilon_-^{*\mu}\epsilon_-^\nu \tag{B.23}$$

Note that $\epsilon_\pm^{*\mu} = \mp\epsilon_\mp^\mu$. While the longitudinal-transverse interference terms are proportional to:

$$\rho_{TL}^{\mu\nu} = -\epsilon_-^{*\mu}\epsilon_0^\nu + \epsilon_0^\mu\epsilon_-^\nu + \epsilon_+^{*\mu}\epsilon_0^\nu - \epsilon_0^\mu\epsilon_+^\nu \tag{B.24}$$

The two expressions are manifestly gauge invariant, antisymmetric and satisfy the necessary crossing relations. The lepton tensor can be written in terms of these densities [73],

$$\mathrm{L}_A^{\mu\nu} = 2Q^2\frac{k_0}{q_3}\left[(1 - \frac{y}{2})\rho_T^{\mu\nu} + \frac{\delta}{2}\rho_{TL}^{\mu\nu}\right] \tag{B.25}$$

where, $\delta = \sqrt{2(1-y) - \frac{y^2}{2}(\frac{q_3^2}{q_0^2} - 1)}$ and $y = \frac{q_0}{k_0}$ is the energy loss. The imaginary component is required to maintain the properties of the tensor under conjugation.

Take for example photoproduction, then the differential cross section given an incident photon with helicity +1 on an unpolarized target is,

$$\frac{d\sigma(+,unpol)}{d\Omega} = \frac{1}{32(2\pi)^3W^2}\frac{|\vec{p}_1|}{|\vec{q}|}\sum_{h_f,h}\tilde{\mathrm{H}}^*_{h_f,1-h}\tilde{\mathrm{H}}_{h_f,1-h} \tag{B.26}$$

$$= \frac{1}{32(2\pi)^3 W^2} \frac{|\vec{p}_1|}{|\vec{q}|} \sum_{i=1}^{4} |\tilde{\mathrm{H}}_i|^2 = \frac{1}{2} \frac{|\vec{p}_1|}{|\vec{q}|} \sum_{i=1}^{4} |\mathrm{H}_i|^2 \tag{B.27}$$

Or for example photoproduction on a polarized target with ±1 helicity photon beam,

$$\frac{d\sigma(+,+)}{d\Omega} - \frac{d\sigma(-,+)}{d\Omega} = \frac{1}{2} \frac{|\vec{p}_1|}{|\vec{q}|} \left[|H_1|^2 - |H_2|^2 + |H_3|^2 - |H_4|^2 \right] \tag{B.28}$$

Any given experimental configuration can easily be given in terms of these amplitudes. The utility of this process resides in the fact that resonances tend to contribute strongly to a particular helicity amplitude. Thus if from spin independent analysis one fits to each resonance a multipole configuration one in principle can predict the spin dependent behavior.

B.2 Breit-Wigner Analysis of Resonances

The analysis performed here is a modification of the work by Walker [20]. Each helicity amplitude is separated into a resonance and Born term,

$$H_i = H_i^R + H_i^B. \tag{B.29}$$

The low J contributions are decomposed into states of definite angular momentum to obtain the interference between the Born and resonance terms. In our case we stopped after reaching $J = 3/2$, as all the prominent resonances are included by this point. The resonances terms for a particular channel are then parameterized by the Breit-Wigner method,

$$H(W)_{i,J}^R = H(W_R, Q^2)_{i,J} \left(\frac{|\vec{p}_{1R}||\vec{q}_R|}{|\vec{p}_1||\vec{q}|} \right) \frac{W_R \Gamma^{\frac{1}{2}} \Gamma_\gamma^{\frac{1}{2}}}{W_R^2 - W^2 - i W_R \Gamma} \tag{B.30}$$

Where the widths are a phenomenological parameterization to get the correct peak shape. They are given by,

$$\Gamma = \Gamma_R \left(\frac{|\vec{p}_1|}{|p_{1R}|} \right)^{2l+1} \left(\frac{|\vec{p}_{1R}|^2 + X^2}{|\vec{p}_1|^2 + X^2} \right)^l \tag{B.31}$$

$$\Gamma_\gamma = \Gamma_R \left(\frac{|\vec{q}|}{|q_R|} \right)^{2h_\gamma} \left(\frac{|\vec{q}_R|^2 + X^2}{|\vec{q}|^2 + X^2} \right)^{h_\gamma} . \tag{B.32}$$

As before, $\vec{p}_1$ and $\vec{q}$ are the pion and photon three momentum respectively. l is the orbital angular momentum of the pion, while h_γ is the helicity of the incident photon. Any quantities with a subscript R are specified at the resonance peak. Γ_R is the resonance width and X is typically a few hundred MeV and controls the peak shape.

The parameterization we used to calculate the polarizability contribution in Chapter Three included the $P33(1232)$, $P11(1440)$, $D13(1520)$, $S11(1535)$, $S11(1650)$, $F15(1680)$, $D31(1700)$ and $F35(1905)$ resonances. Using the total angular momentum J and the orbital angular momentum of the pion decay channel as specified in the Particle Data Book [30], the contribution of each resonance at its pole was decomposed into Walker helicity amplitudes as a function of Q^2. Isospin considerations where added through the use of appropriate Clebsch-Gordon coefficients. For the delta and some other prominent resonances these amplitudes have been extracted from experiment, while reasonable parameterizations have been used for the weaker resonances [23]. The values for X were taken from the photoproduction work of Walker [20]. Due to the known isospin problems with pion photoproduction data outlined in Chapter Three, we neglected the isovector-isosinglet interference term. This term has an opposite sign at the photoproduction point than would be expected from the DHG sum rule. This is most likely due to the small size of the singlet channel; the isosinglet-isosinglet piece only contributes $\approx 1 - 2\%$ at the photoproduction point to the total. The resultant parameterization undersaturated the DHG sum rule by about 30%, we therefore provided an overall normalization factor to force saturation.

Appendix C

Algebraic Conventions

The notation used in this thesis is primarily that of Itzykson and Zuber [9]. A brief table of useful formula follows:

The antisymmetric tensor is given by,

$$\epsilon^{0123} = 1 = -\epsilon_{0123} \tag{C.1}$$

The low energy representation used for the Dirac matrices,

$$\gamma^0 = \begin{pmatrix} I & 0 \\ 0 & -I \end{pmatrix} \tag{C.2}$$

$$\gamma^i = \begin{pmatrix} 0 & \sigma_i \\ -\sigma_i & 0 \end{pmatrix} \tag{C.3}$$

$$\gamma^5 = \begin{pmatrix} 0 & I \\ I & 0 \end{pmatrix} \tag{C.4}$$

The anticommutative relation for the Dirac matrices,

$$\{\gamma^\mu, \gamma^\nu\} = 2g^{\mu\nu} \tag{C.5}$$

The cyclic property of the Dirac matrices.

$$\gamma^\alpha \gamma^\beta \gamma^\mu = S^{\alpha\beta\mu\nu}\gamma_\nu + i\epsilon^{\alpha\beta\mu\nu}\gamma_\nu\gamma_5 \tag{C.6}$$

where

$$S^{\alpha\beta\mu\nu} = g^{\alpha\beta}g^{\mu\nu} - g^{\alpha\mu}g^{\beta\nu} + g^{\alpha\nu}g^{\beta\mu} \tag{C.7}$$

Trace and antisymmetric properties,

$$Tr(\gamma^5\gamma^\alpha\gamma^\beta\gamma^\mu\gamma^\nu) = -4i\epsilon^{\alpha\beta\mu\nu} \tag{C.8}$$

$$Tr(\gamma^\alpha\gamma^\beta\gamma^\mu\gamma^\nu) = 4S^{\alpha\beta\mu\nu} \tag{C.9}$$

$$g^{\lambda\delta}\epsilon^{\mu\nu\alpha\beta} = g^{\mu\delta}\epsilon^{\lambda\nu\alpha\beta} + g^{\nu\delta}\epsilon^{\mu\lambda\alpha\beta} + g^{\alpha\delta}\epsilon^{\mu\nu\lambda\beta} + g^{\beta\delta}\epsilon^{\mu\nu\alpha\lambda} \tag{C.10}$$

In addition the following commutator relations of the total derivatives where found to be useful,

$$[iD^\mu, iD^\nu] = -igF^{\mu\nu} \tag{C.11}$$

$$\{i\not{D}, \gamma^\mu\} = 2iD^\mu \tag{C.12}$$

C.1 Rotation Matrices

The rotation matrix is given implicitly by:

$$\begin{aligned} d^j_{m'm}(\beta) &= \sum_k (-1)^{k-m+m'} \frac{\sqrt{(j+m)!(j-m)!(j+m')!(j-m')!}}{(j+m-k)!(j-m'-k)!(k-m+m')!k!} \\ &\cdot \cos(\frac{\beta}{2})^{2j-2k+m-m'} \sin(\frac{\beta}{2})^{2k-m+m'} \end{aligned} \tag{C.13}$$

$$d^j_{m'm}(\beta) = (-1)^{m'-m} d^j_{-m'-m} \tag{C.14}$$

$$d^j_{m'm}(\beta) = (-1)^{m'-m} d^j_{mm'} \tag{C.15}$$

The form of the rotation matrix that we are particularly interested is given as follows,

$$D(\alpha, \beta, -\alpha)^{j}_{m'm} = e^{i\alpha(m-m')} d^{j}_{m'm}(\beta) \tag{C.16}$$

Appendix D

Fundamental Constants

For ease of reference, the results calculated in Chapter Two and Three made use of the following constants, the uncertainties being in parts per billion:

Constant	Value	ppb
m_p	$1.007\ 276\ 466\ 6(6)\ u$	0.6
m_e	$5.485\ 799\ 111(12) \times 10^{-4}\ u$	2.2
m_μ	$0.113\ 428\ 913(17)\ u$	150
κ_p	$1.792\ 847\ 386(63)$	35
κ_e	$1.159\ 652\ 193(10) \times 10^{-3}$	8.6
κ_μ	$1.165\ 923\ 0(84) \times 10^{-3}$	7200
R_∞	$10\ 973\ 731.570\ 9(18)\ \mathrm{m}^{-1}$	0.16
$1/\alpha$	$137.035\ 989\ 5(61)$	45
c	$299\ 792\ 458\ \mathrm{m/s}$	exact

The constants in this table where taken from reference [30]. The electron and proton mass are from [28], the Rydberg is from [10].

Bibliography

[1] D.J. Berkeland, E.A. Hinds, and M.G. Boschier, Phys. Rev. Lett. **75**, 2470 (1995).

[2] E.W. Hagley and F.M. Pipkin, Phys. Rev. Lett. **72**, 1172 (1994).

[3] M. Weitz, et al. Phys. Rev. Lett. **72**, 328 (1994).

[4] K. Pachucki and H. Grotch, Phys. Rev. A **51**, 1854 (1995).

[5] K. Pachucki, Phys. Rev. A **52**, 1079 (1995).

[6] L.N. Hand et al. Rev. Mod. Phys. **35**, 335 (1963).

[7] G.G. Simon et al., Nuc. Phys. A **333**, 381 (1980).

[8] J.J. Sakurai, Advanced Quantum Mechanics, Addison Wesley, (1967).

[9] C. Itzykson and J.B. Zuber, Quantum Field Theory, McGraw-Hill, (1980).

[10] K. Jungmann, V.W. Hughes and G. zu Pulitz (Eds.), The Future of Muon Physics, Springer-Verlag, (1992).

[11] T. Kinoshita and M. Nio, Phys. Rev. Lett. **72**, 3803 (1994).

[12] G.T. Bodwin and D.R. Yennie, Phys. Rev. D **37**, 498 (1988).

[13] P.Gnadig and J. Kuti, Phys. Lett. B **37**, 201 (1971).

[14] S.B. Crampton, D. Kleppner and N. F. Ramsey, Phys. Rev. Lett. **11**, 338 (1963).

[15] L. Essen et al., Nature, **229**, 110 (1971).

[16] V. Hughes and J. Juti, Ann. Rev. Nucl. Part. Sci. **33**, 611 (1983).

[17] S.D. Drell and J. D. Sullivan, Phys. Rev. **154**, 1477 (1967).

[18] W.E. Caswell and G.P. Lepage, Phys. Rev. Lett. **41**, 1092 (1978).

[19] V.B. Berestetskii, E.M. Lifshitz and L.P. Pitaevskii, Quantum Electrodynamics, Pergamon Press, 1980.

[20] R.L. Walker Phys. Rev **182**, 1729 (1969).

[21] F. Foster and G. Hughes, Reports on Progress in Physics **46**, 1445, (1983).

[22] V. Burkert and L. Elouadrhiri, Phys. Rev. Lett. **75**, 3614 (1995).

[23] V. Burkert and Z. Li, Phys. Rev. D **47**, 46 (1993), and V. Burkert personal communication.

[24] I. Karliner, Phys. Rev. D **7**, 2717 (1973).

[25] R.L. Workman and R.A. Arndt, Phys. Rev D **45**, 1789 (1992).

[26] A. M. Sandorfi et al., Phys. Rev. D **50**, R6681 (1994).

[27] K. Abe et al, SLAC-PUB-95-6982 to appear in Phys. Rev. Lett.

[28] D. L. Farnham, R.S. Van Dyck and P.B. Schwinberg, Phys. Rev. Lett. **75**, 3598 (1995).

[29] D.R. Yennie, Z. Phys. C - Particles and Fields **56**, S13 (1992).

[30] Review of Particle Properties, Phys. Rev. D **50** (1994).

[31] T. Muta, Foundations of Quantum Chromodynamics, World Scientific, Singapore, (1987).

[32] F.J. Ynduráin, Quantum Chromodynamics, Springer-Verlag, New York, (1983).

[33] J. Schwinger, Particles, Sources and Fields, Addison-Wesley, Reading, (1970).

[34] A.J. Buras, Review of Modern Physics, **52**, 199 (1980).

[35] D.J. Gross and F. Wilczek, Phys. Rev. **D8**, 3633 (1973).

[36] J.D. Bjorken, Phys. Rev. **148**, 1467 (1966).

[37] J. Ellis and R.L. Jaffe, Phys. Rev. **D9**, 1444 (1974).

[38] The EMC Collaboration, J. Ashman et al., Nucl. Phys. **B328**, 1 (1989).

[39] The E142 Collaboration, P. L. Anthony et al., Phys. Rev. Lett. **71**, 959 (1993).

[40] The SMC Collaboration, B. Adeva et al., Phys. Lett. **B302**, 533 (1993).

[41] M. Anselmino, B. L. Ioffe, and E. Leader, Sov. J. Nucl. Phys. **49**, 136 (1989).

[42] S. D. Drell and A. C. Hearn, Phys. Rev. Lett. **16**, 908 (1966); S. B. Gerasimov, Sov. J. Nucl. Phys. **2**, 430 (1966).

[43] J. Ahrens, Mainz proposal 12/2-93, (1993); G. Anton, Bonn proposal, (1992).

[44] V. Burkert et al., CEBAF proposal 91-023, (1991); S. E. Kuhn et al., CEBAF Proposal, (1993).

[45] X. Ji, Phys. Lett. **309B**, 187 (1993).

[46] J. Kodaira, S. Matsuda, K. Sasaki, and T. Uematsu, Nucl. Phys. **B159**, 505 (1979); J. Kodaira, Nucl. Phys. **B165**, 129 (1980).

[47] S. A. Larin, F. V. Tkachev, and J. A. M. Vermaseren, Phys. Rev. Lett. **66**, 862 (1991).

[48] E. Shuryak and A. Vainshtein, Nucl. Phys. **B199**, 451 (1982); Nucl. Phys. **B201**, 141 (1982).

[49] R. K. Ellis, W. Furmanski, and R. Petronzio, Nucl. Phys. **B212**, 29 (1983).

[50] X. Ji, Nucl. Phys. **B402**, 217 (1993).

[51] R. L. Jaffe, Phys. Rev. **D11**, 1953 (1975).

[52] R. L. Jaffe and X.Ji, Phys. Rev. **D43**, 724 (1991).

[53] I. I. Balitsky, V. M. Braun, and A. V. Kolesnichenko, JETP Lett. **50**, 61 (1989); Phys. Lett. **242B**, 245 (1990); Erratum, hep-ph/9310316, (1993).

[54] J. Ellis and M. Karliner, Plenary talk at the 13th International Conference on Particles and Nuclei, PANIC'93, July (1993), Perugia, Italy.

[55] E. D. Bloom and F. J. Gilman, Phys. Rev. D **4**, 2901 (1971).

[56] A. de Rujula, H. Georgi, and H. D. Politzer, Ann. Phys. **103**, 315 (1977).

[57] C. E. Carlson and N. C. Mukhopadhyay, Phys. Rev. D **47**, R1737 (1993).

[58] A. J. Buras, Rev. Mod. Phys. **52**, 199 (1980).

[59] E. V. Shuryak and A. I. Vainshtein, Nucl. Phys. **199**, 451 (1982); R. L. Jaffe and M. Soldate, Phys. Rev. D **26**, 49 (1982); R. R. Ellis, W. Furmanski, and R. Petronzio, Nucl. Phys. B **212**, 29 (1983).

[60] M. A. Shifman, A. I. Vainshtein, and V. I. Zakharov, Nucl. Phys. B **147**, 385, 447 (1979).

[61] M. Virchaux, in QCD, 20 years later, ed. by P. M. Zerwas and H. A. Kastrup, (1992).

[62] A. Mueller, Phys. Letts. B **308**, 355 (1993).

[63] F. W. Brasse et al. Nucl. Phys. B **110**, 413 (1976).

[64] A. Bodek et al. Phys. Rev. D **20**, 1471 (1979).

[65] M. Virchaux and A. Milsztajn, Phys. Lett. B **274**, 221 (1992).

[66] The New Muon Collaboration, P. Amaudruz et al. Phys. Lett. B **295**, 159 (1992).

[67] The CTEQ2 distribution, by J. Botts, J. Huston, H. L. Lai, J. G. Morfin, J. F. Owens, J. Qiu, W. K. Tung, and H. Weerts. (1994).

[68] The Particle Data Book, (1992) edition; G. Altarelli, in QCD, 20 years later, ed. by P. M. Zerwas and H. A. Kastrup, (1992).

[69] H. Georgi and H. D. Politzer, Phys. Rev. D **14**, 1829 (1976).

[70] A. Chodos, R.L. Jaffe, K. Johnson and C.B. Thorn Phys. Rev. D **11**, 2599 (1974).

[71] R.J. Hughes, Phys. Rev. D **16**, 622 (1977).

[72] R.L. Jaffe and X. Ji, Phys. Rev. D **43**, 724 (1991).

[73] R.L. Jaffe and A. Manohar, Nucl. Phy. B **321**, 343 (1989).